J. Fluid Mech. (2007), vol. 576, pp. 27–61. © 2007 Cambridge University Press
doi:10.1017/S0022112006004575 Printed in the United Kingdom

Langmuir turbulence in shallow water. Part 1. Observations

ANN E. GARGETT AND JUDITH R. WELLS

Center for Coastal Physical Oceanography, Department of Ocean, Earth and Atmospheric Sciences, Old Dominion University, Norfolk, VA 23529, USA

(Received 20 October 2005 and in revised form 13 October 2006)

During extended deployment at an ocean observatory off the coast of New Jersey, a bottom-mounted five-beam acoustic Doppler current profiler measured large-scale velocity structures that we interpret as Langmuir circulations filling the entire water column. These circulations are the large-eddy structures of wind-wave-driven turbulent flows that occur episodically when a shallow water column experiences prolonged strong wind forcing. Many observational characteristics agree with former descriptions of Langmuir circulations in deep water. The three-dimensional velocity field reveals quasi-organized structures consisting of pairs of surface-intensified counter-rotating vortices, aligned approximately downwind. Maximum downward velocities are stronger than upward velocities, and the downwelling region of each cell, defined as a pair of vortices, is narrower than the upwelling region. Maximum downward vertical velocity occurs at or above mid-depth, and scales approximately with wind speed. The estimated crosswind scale of cells is roughly 3–6 times their vertical scale, set under these conditions by water depth. The long axis of the cells appears to lie at an angle $\sim 10^{\circ}$–20° to the right of the wind. A major difference from deep-water observations is strong near-bottom intensification of the downwind 'jets' found typically centred over downwelling regions. Accessible observational features such as cell morphology and profiles of mean velocities, turbulent velocity variances, and shear stress components are compared with the results of associated large-eddy simulations (reported in Part 2) of shallow water flows driven by surface stress and the Craik–Leibovich vortex forcing generally used to represent generation of Langmuir cells. A particularly sensitive diagnostic for identification of Langmuir circulations as the energy-containing eddies of the turbulent flow is the depth trajectory of invariants of the turbulent stress tensor, plotted in the Lumley 'triangle' corresponding to realizable turbulent flows. When Langmuir structures are present in the observations, the Lumley map is distinctly different from that of surface-stress-driven Couette flow, again in agreement with the large-eddy simulations (LES). Unlike the LES, observed velocity fields contain two distinct and significant scales of variability, documented by wavelet analysis of observational records of vertical velocity. Variability with periods of many minutes is that expected from Langmuir cells drifting past the instrument at the slowly time-varying crosswind velocity. Shorter period variability, of the order of 1–2 min, has roughly the observed periodicity of surface wave groups, suggesting a connection with the wave groups themselves and/or the wave breaking associated with them in high wind conditions.

1. Introduction

The existence of large-scale semi-organized structures in the wind-driven surface boundary layers of lakes and oceans has long been recognized. During a crossing

of the North Atlantic in 1927, Irving Langmuir realized that the long lines of floating Sargassum weed that he observed lined up approximately downwind had to be associated with periodic surface convergence zones in the surface-layer flow. If downwind flow does not increase sufficiently within the bands (and he later showed that it does not), continuity requires that such convergences supply regions of downwelling flow beneath the surface bands, with compensating upward flows between bands. Langmuir (1938) subsequently verified the existence of his proposed arrays of counter-rotating line vortices beneath the water surface with a series of observations in Lake George, New York. In the decades since his pioneering work, the circulations named after him have been studied by a variety of means, including laboratory studies (Faller & Caponi 1978), observations (Smith, Pinkel & Weller 1987; Zedel & Farmer 1991), theoretical studies (Craik & Leibovich 1976; Gnanadesikan 1996) and numerical modelling (Skyllingstad & Denbo 1995; McWilliams, Sullivan & Moeng 1997; Li, Garrett & Skyllingstad 2005). The papers cited here are a small selection from a large literature on the subject; further references are found within the text, and more complete coverage of the evolving literature can be found in reviews by Pollard (1976), Leibovich (1983) and Thorpe (2004).

It is generally believed that Langmuir circulations (LC) are generated when the Stokes drift associated with finite-amplitude surface gravity waves strains vertical vorticity associated with irregularities in wind-driven 'mean' currents into the horizontal downwind direction, giving rise to a vortex force (the so-called C-L force, Craik & Leibovich 1976) in wave-period-averaged equations of motion. Most field studies of Langmuir circulations have taken place in deep water, where cell size is not limited by depth. These studies have determined a number of features that are accepted as characteristic of the presence of LC in this environment. Maximum downwelling velocity w_{dn} occurs at or above mid-depth in the cells and exceeds the maximum upwelling velocity (Smith *et al.* 1987; Weller & Price 1988), hence upwelling limbs of cells are wider than downwelling limbs. Horizontal scales of Langmuir cells (here defining a cell as a vortex pair) are roughly three times the vertical scale (Smith *et al.* 1987). 'Jets' of enhanced downwind flow are associated with downwellings (Langmuir 1938; Smith *et al.* 1987; Weller & Price 1988).

In contrast to the deep-water literature, there are surprisingly few reports of LC in shallow coastal waters where, given observed depths of penetration offshore, the cells might reasonably be expected to reach, hence potentially interact with, the bottom. A first report may be that of Van Straaten (1950), who described striking features parallel to a 'moderate' wind in the very shallow water (10–40 cm) of a Dutch tidal area:

> On the surface there were regularly spaced sets of smooth streaks, in which the scarce foam was concentrated. The motion in the water itself was rendered directly visible by the presence of large quantities of rather coarse, suspended mud flakes. This suspended mud was homogeneously distributed in the zones of rising water, halfway between the streaks of smooth water. Below these latter streaks however, the lines of descent themselves were conspicuous by their relatively clear water.

In the subsequent decades, there are only two reports of large-scale banded structures in shallow waters, both from aerial observations. Off the coast of Texas, Hunter & Hill (1980) observed elongated streaks in water colour, lined up roughly downwind, and argued that the light streaks resulted from sediment raised from the bottom in the upwelling regions of LC. Marmorino, Smith & Lindemann (2005) reported similar banded structures in remotely sensed sea surface temperature observed off the Gulf coast of Florida, and again suggested that these surface

signatures resulted from the action of LC. Both studies found streak spacing (equal to the horizontal size of a Langmuir cell) of the order of 10 times the vertical cell size (in both cases taken as equal to the water depth), which is considerably larger than the spacing of roughly 3 times the vertical scale that has been found typical in deep waters, or that of 4–5 reported by Van Straaten. Unfortunately, neither study was accompanied by in-water observations necessary to confirm that the underlying features were indeed LC. This paper describes such observations: measurements of the full three-dimensional velocity field associated with Langmuir circulations that engulf the entire water column during prolonged strong wind forcing of the shallow continental shelf off the coast of New Jersey. Gargett *et al.* (2004) called these full-depth Langmuir circulations Langmuir supercells (LSC), in tribute to their major impact on the horizontal transport of sediment and bioactive material in shallow-shelf seas.

It has been clear for some time that there is a hierarchy of scales present in LC under natural wind/wave forcing (Smith *et al.* 1987; Plueddemann *et al.* 1996), moreover that scales evolve with time, not only under changing forcing, but also under apparently constant wind/wave conditions (Smith 1992). In the most general sense, it seems appropriate to consider naturally occurring LC as a turbulent flow in which the largest scales of LC are the energy-containing eddies, albeit somewhat better organized than the large eddies of a more usual turbulent flow. This view has been encouraged by the success of large-eddy simulations (LES) of fully nonlinear turbulent flows under C-L vortex forcing (Skyllingstad & Denbo 1995; McWilliams *et al.* 1997; Li *et al.* 2005) in reproducing many of the observed flow characteristics typical of deep-water LC. Taking this point of view, the present paper focuses on identification of LSC as the dominant large eddies of Langmuir turbulence, using comparisons between various accessible observational characteristics and results of previous observational and theoretical studies. We also refer frequently to a companion LES study of Langmuir turbulence in shallow water (Tejada-Martínez & Grosch 2007, hereinafter referred to as Part 2), in which the basic (non-rotating) case uses forcing functions scaled with the wind stress and surface wave characteristics of our observations.

Although our observations encompass all phases of LC development and decay, the present paper treats only observations in which full-depth LSC are observed under quasi-steady wind/wave forcing. Section 2 describes the observational site and the dramatic sediment resuspension events that were the most striking features observed during 6.5 months of continuous data recording. Section 3 describes the five-beam acoustic Doppler current profiler (VADCP) used to measure mean and turbulent velocity fields, as well as the ancillary data sets used in their interpretation. Section 4 reviews techniques used to derive turbulence characteristics from VADCP data and addresses various issues associated with use of the data. Section 5 presents observational features used to diagnose LC, incorporating comparisons with the companion LES. The presence of two significant scales of variability in the observations, rather than the single dominant scale present in the simulations, is documented and discussed in §6, and we conclude in §7 by considering the major remaining questions associated with, and possible consequences of, the episodic occurrence of full-depth Langmuir circulations in shallow coastal seas.

2. Observations

LEO-15, a cabled ocean observatory located off the New Jersey coast of the United States provides instrument power and data transmission at two underwater

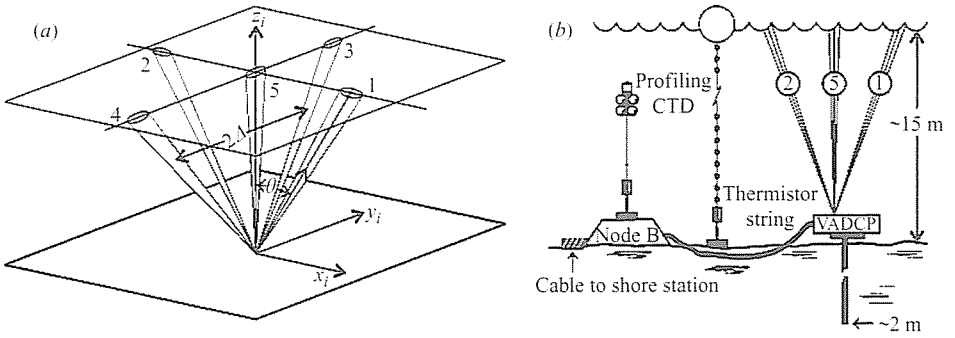

FIGURE 1. (*a*) Bottom-mounted upward-looking 5-beam VADCP. Slant beams make an angle of $\theta = 30^\circ$ from vertical. Horizontal separation of the slant beam pairs $2\Delta = 2z_i \tan\theta$ increases with distance z_i above the transducer. (*b*) Instrumentation installed at the LEO-15 ocean observatory off the coast of New Jersey between 22 April and 31 October 2003. The VADCP was located ~48 m to the NNE, and the thermistor chain ~95 m to the SE, of the node.

nodes.† The deepest node (B: 39° 27.69′N, 74° 14.68′W)) is in water of 15 m average depth, approximately 7 km from a wave-exposed shoreline oriented roughly 30–40° to the east of true north. A predominantly sand and clay bottom slopes gently shoreward. In the vicinity of the deployment site, southwesterly annual mean flow in the region is steered slightly offshore by a low topographic bump just to the south (Kohut, Glenn & Chant 2004).

Prolonged storm winds during early spring and autumn seasons come predominantly from the NE (hence the local name nor'easter). The near-shore water column is well mixed during the winter, but strongly stratified by wind-driven upwelling and solar heating during the summer. Transition from summer to winter stratification occurs relatively abruptly, usually in early September, with a decisive switch from upwelling- to downwelling-favourable winds. Development of springtime stratification is a slower process, a combination of increasing solar heating, riverine freshwater inputs, and the occasional upwelling event. Periods of spring stratification frequently revert to mixed conditions as a result of downwelling and mixing associated with nor'easters.

On 15 April 2003, a 1.2 MHz vertical-beam acoustic Doppler current profiler was installed in the bottom-mounted upward-looking configuration shown in figure 1. Beam velocities and backscatter amplitudes were recorded continuously at a sample rate of $\sim 1\,\mathrm{s}^{-1}$ from 22 April to 31 October 2003, a period spanning the full annual ranges of thermal and tidal forcing, and a range of wind forcing that included a minor hurricane. The most striking observations throughout this period were of episodic events in which strong backscatter plumes originating from the bottom were observed to extend through the full water column. The backscatter record in figure 2(*a*) illustrates such an event, associated with a nor'easter that lasted for more than a day in mid-May. In the compressed view of figure 2(*a*), the high backscatter observed throughout the water column between ~1300Z 16 May and 0000Z 18 May appears nearly continuous. However, expansion of such records reveals separated regions of high backscatter originating near-surface and near-bottom,

† For location and topography, see http://marine.rutgers.edu/mrs/LEO/LEO15.html.

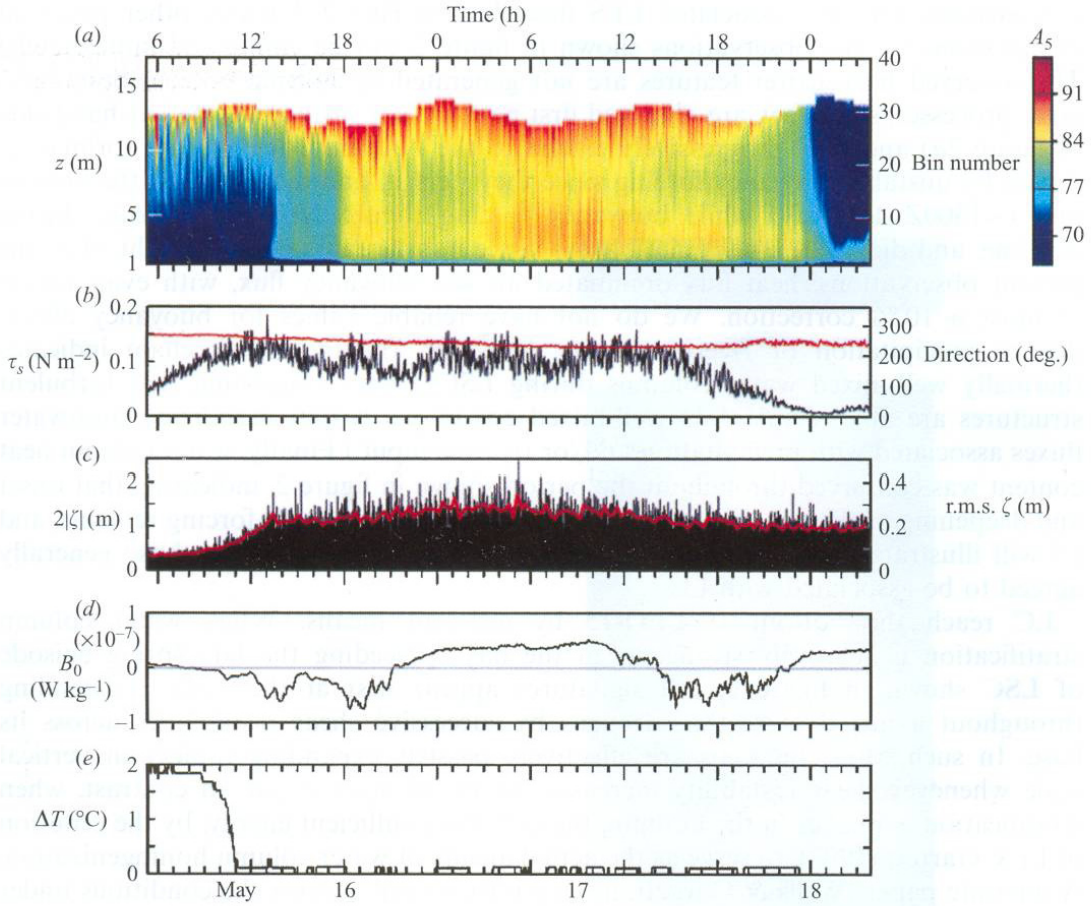

FIGURE 2. An episode of Langmuir supercells, beginning ~1300 16 May 2003 and ending ~0000 18 May 2003. (*a*) Backscatter amplitude (corrected for transmission loss and beam spread but uncalibrated) from the vertical beam (A_5), units are relative. Associated time series of variables related to water column forcing. (*b*) Wind stress τ_s (black) and direction (red) *to which* the wind is blowing. (c) Instantaneous height $2|\zeta|$ (black) and root mean square height r.m.s. ζ averaged over 16 min intervals (red, note difference in scale) of shallow-water surface waves, calculated from bottom pressure. (d) B_0, buoyancy flux due to heat (positive for (destabilizing) ocean heat loss). (*e*) Top to bottom water column temperature difference (positive is stable), the difference between records of the top sensor on the thermistor chain and the bottom temperature sensor on the node.

regions respectively highly correlated with downwards and upwards vertical velocities measured by the vertical beam of the VADCP (cf. figures 6 and 13). The surface-origin backscatter signatures are similar to those previously documented as scattering from air microbubbles deposited near-surface by wave breaking and redistributed to depth in the downwelling limbs of LC (Thorpe & Hall 1983; Zedel & Farmer 1991). We interpret the backscatter clouds originating from the bottom as being due to resuspended sediment moved towards the surface in the upwelling limbs of LC that extend over the full depth of the water column. The backscatter record indicates that some component of the resuspended sediment reaches very near the surface, confirming anecdotal reports of sand caught in surface water bottle samples taken in this region during nor'easters (L. Atkinson, personal communication).

Identification of these observations as full water depth Langmuir circulations results from examination of forcing fields and in-water observational data, combined with

comparisons with the associated LES described in Part 2. Various other potential explanations for the observations shown in figure 2 can be eliminated immediately. The observed backscatter features are not generated by normal bottom boundary-layer processes, since they are observed first near the sea surface (to the left-hand side of figure 2*a*) and only progressively extend to the bottom. They are not (primarily) driven by unstable buoyancy forcing since they persist, and indeed reach the bottom first (~1300Z 16 May) while buoyancy forcing (figure 2*d*) is stabilizing during daytime, and die away (~0000Z 18 May) while it is destabilizing overnight. (For the present observations, heat flux dominated air–sea buoyancy flux, with evaporation at most a 10% correction. We do not have reliable values for buoyancy effects due to precipitation or riverine inputs. However, the thermistor chain indicates thermally well-mixed water columns during LSC events, suggesting that turbulent structures are able to maintain well-mixed conditions despite stabilizing freshwater fluxes associated with precipitation and/or riverine input.) Finally, water column heat content was conserved throughout the period shown in figure 2, indicating that onset and deepening of the features are not advective effects. Langmuir forcing remains, and § 5 will illustrate characteristics of the observations that agree with those generally agreed to be associated with LC.

LC reach the bottom at LEO-15 by different means. When water column stratification is relatively strong, as in the days preceding the late spring episode of LSC shown in figure 2, cell signatures appear first at the surface, extending throughout a mixed layer that deepens by successive shear instabilities across its base. In such cases, the cells are effectively passive, expanding rapidly in vertical scale whenever shear instability increases the mixed-layer depth. In contrast, when stratification is weaker in the autumn, the cells have sufficient energy, by the criterion of Li & Garrett (1997), to serve as the actual agents of water column homogenization. A separate paper (Wells & Gargett, in preparation) will address the conditions under which LC form, deepen (or not) to full depth, and decay: this paper focuses on the quasi-steady-state characteristics of LC that have achieved full depth, by whatever means.

3. Instrumentation

The VADCP is a broadband instrument (RD Instruments) with a vertical transducer added to the centre of four standard slant beams, each angled 30° from vertical in a Janus configuration (figure 1*a*). The instrument was bolted to a plate attached to a 2 m hollow post. This platform, 'jetted' into the sandy bottom using water pressure from a ship's firehose, proved extremely stable. After the Doppler vertical beam was adjusted to vertical (within $\pm 0.1°$) by divers, pitch and roll output did not vary from zero by more than $\pm 0.2°$ until 18 September, when roll increased to 0.5° during the passage of a hurricane: divers readjusted the instrument to vertical on 24 September. The VADCP was operated in RDI Mode 4 which produces velocity measurements with noise dominated by Doppler 'self-noise', independent of the flow being measured. The basic measurements are velocities along the acoustic beams, with beam velocity towards the transducer defined as positive. Backscatter amplitude from the vertical beam, corrected for the (relative) effects of beam spreading and transmission losses, serves to image turbulent flow structures that carry acoustic targets. Because the transducer was not calibrated, no quantitative measures of backscatter strength are possible.

Much of the LEO-15 deployment used a standard set of sampling characteristics that incorporated the usual tradeoffs among range and vertical and temporal

resolutions, subject to two constraints. First, full water column coverage was deemed essential for understanding the 'mean' setting of any observed turbulent processes. Secondly, the sample period had to be short enough to avoid aliasing large velocities associated with ever-present surface waves: typical wind-generated wave periods of 6–8 s at the site suggested that a sample period of ~1 s was adequate. With these constraints, vertical resolution (bin size) of 0.4 m was achieved. Since the instrument remained vertical, the distance of an acoustic bin above the transducer is easily determined. However, bottom sediments are mobile and we have only two measurements of the height of the transducer above the bottom during the deployment, 0.57 m on 25 April and 0.66 m on 10 July. Since these dates are separated by some major LSC events and associated sediment movement, the two available measurements suggest that uncertainty in the heights of the bins above the bottom is of the order of ± 10 cm.

The VADCP data stream was broken into sessions containing multiple records, each of length ~2.3 h. Over this period, about 1/5 of the dominant semi-diurnal tidal period at LEO-15, the 'mean' (including tidal) flow may be considered at least quasi-stationary, a point addressed further in § 4. Individual records will be referenced as a combination of session number and record number within the session: e.g. 43.025 is session 43, record number 25.

Various ancillary data sets are crucial for interpretation of the VADCP velocity field observations. A thermistor chain (figure 1*b*), sampled at 4 min intervals, was moored below a surface buoy approximately 95 m to the SE of the node. The chain was made up of two thermistors located on the surface mooring at 0.25 and 0.50 m below the surface, with deeper thermistors spaced along the mooring chain at 0.25 m intervals from 1.75 to 13 m below surface. The difference between the temperature from the uppermost thermistor on this chain and that from a bottom temperature measurement at the node is used as a rough indicator of water column stability (figure 2*e*). When more accuracy is required in water column stability, the (highly variable) temperature–salinity relationship determined by sporadic profiles taken at the node can be used to convert from temperature to density. Pressure is measured at the node at 1 s intervals: a high-pass version of this record is used to estimate the surface wave height ζ, shown in figure 2(*c*) as calculated for shallow-water waves. The actual dominant surface waves at LEO-15 are of intermediate class, i.e. neither deep-water nor shallow-water waves. In such cases, heights shown in figure 2(*c*) require corrections (by factors up to 2) which depend upon dominant surface wave period: corrections are carried out for individual records when quantitative measures are required. Essential meteorological variables were measured on a tower that stands on the shoreline ~7 km to the west of the deployment site. The tower has excellent exposure to onshore winds, which include the nor'easters that typically generate LSC, and comparison of tower wind speed and direction with those measured at an offshore buoy in the vicinity shows a high degree of correlation (Münchow & Chant 2000). Relative humidity (%), air temperature (°C), wind speed and direction (using the oceanic convention of direction to which the wind is blowing), and shortwave insolation ($W\,m^{-2}$) were reported from a 10 m height every minute. Wind stress and surface buoyancy flux (positive if the ocean is losing buoyancy) are derived from these variables using standard algorithms.†

† Available at http://woodshole.er.usgs.gov/operations/sea-mat/air_sea-html

4. Deriving turbulence quantities from a VADCP

4.1. *Theory*

Let the three-dimensional velocity field be $\boldsymbol{u}(x_i, y_i, z_i) = (u, v, w)$ in an instrument-based coordinate system with the origin at the transducer face(s), x_i positive in the direction from beam 2 towards beam 1, y_i positive from beam 4 towards beam 3, and z_i positive upwards. With the VADCP mounted in the upward-looking configuration of figure 1(*a*) and adjusted to vertical, the vertical beam provides unequivocal measurements of vertical velocity as a function of z_i at the centre of the array of acoustic beams

$$B_5 = -w(0, 0, z_i). \tag{1}$$

Slant beam velocities at height z_i are given by

$$B_1 = -u(+\Delta(z_i), 0, z_i)\sin\theta - w(+\Delta(z_i), 0, z_i)\cos\theta, \tag{2}$$

$$B_2 = u(-\Delta(z_i), 0, z_i)\sin\theta - w(-\Delta(z_i), 0, z_i)\cos\theta, \tag{3}$$

$$B_3 = -v(0, +\Delta(z_i), z_i)\sin\theta - w(0, +\Delta(z_i), z_i)\cos\theta, \tag{4}$$

$$B_4 = v(0, -\Delta(z_i), z_i)\sin\theta - w(0, -\Delta(z_i), z_i)\cos\theta, \tag{5}$$

where $2\Delta(z_i) = 2z_i\tan\theta$ is the horizontal spacing between beam pairs at height z_i. Under an assumption of *first-order homogeneity* over the full beam spread, i.e. that velocity structures have horizontal scale much larger than the distance 2Δ between the beams such that $u_i(-\Delta, 0, z_i) = u_i(\Delta, 0, z_i)$ and $v_i(0, +\Delta, z_i) = v_i(0, -\Delta, z_i)$, slant beam velocities can be used to make what we will call first-order full-spread (subscript $1F$) estimates of horizontal velocity components

$$u_{1F} = \frac{B_2 - B_1}{2\sin\theta}, \tag{6}$$

$$v_{1F} = \frac{B_4 - B_3}{2\sin\theta}, \tag{7}$$

and of vertical velocity

$$w_{1F} = -\frac{\sum_{i=1}^{4} B_i}{4\cos\theta} \tag{8}$$

as functions of height above the transducer z_i. (Vertical beam measurements of vertical velocity extend to the instantaneous surface at $z_i = R$, where R is the range of the surface above the vertical transducer, a distance easily determined (within ± 0.2 m) from the strong surface return in vertical beam backscatter. Returns from the surface in vertical sidelobes of the slant beams have the potential to contaminate slant beam estimates (6)–(8) when $z_i > z_s = 0.85R$. However, while we easily identify sidelobe contamination in the slant beam velocities when the sea surface is calm, it is not easily discernible at times when the surface is strongly wind/wave forced, as it is during LSC episodes. Thus for the present investigation, we compute and use horizontal as well as vertical velocities up to the (minimum) sea surface, while still noting the vertical location of potential sidelobe effects in fields derived from slant beam velocities.)

In a statistically stationary turbulent flow, instantaneous water velocity $\boldsymbol{u} = \boldsymbol{U} + \boldsymbol{u}'$ is generally assumed to consist of two parts, a mean (The question of how to determine an appropriate mean in a time-varying flow such as the tidally-dominated flow at LEO-15 is a difficult one, of long standing in the turbulence literature. Section 4.2.2 outlines the process by which a 'mean' is defined and removed in this analysis.)

field $\boldsymbol{U}(z_i)=(\boldsymbol{U}(z_i), \boldsymbol{V}(z_i), 0)$ that is a function only of z_i, and a three-dimensional fluctuating field $\boldsymbol{u}'$ with zero mean $\langle \boldsymbol{u}' \rangle = 0$ and (turbulent) kinetic energy per unit mass $E=(1/2)\langle u'u' + v'v' + w'w' \rangle$, where angle brackets denote a suitable averaging process. In this case, the beam velocities $B_q = \langle B_q \rangle + B_{qf}$ are also made up of two parts, a mean $\langle B_q(z_i) \rangle$ and a turbulent part B_{qf} with zero mean $\langle B_{qf} \rangle = 0$ and variance $\langle B_{qf}^2 \rangle$. Expressions for $\boldsymbol{U}$ and $\boldsymbol{V}$ are versions of (6) and (7) with B_q replaced by $\langle B_q(z_i) \rangle$, while expressions for the turbulent parts of the beam velocities are (1)–(5) with B_q replaced by B_{qf} and (u, v, w) replaced by (u', v', w'). Assuming first-order full-spread homogeneity at the scale of the stress-containing eddies of the turbulent part of the flow, turbulent shear stresses can be calculated as

$$\langle -u'w' \rangle_{1F} = \frac{\langle (B_{f2} - B_{f1}) \Sigma B_{fi} \rangle}{4 \sin 2\theta} \tag{9}$$

$$\langle -v'w' \rangle_{1F} = \frac{\langle (B_{f4} - B_{f3}) \Sigma B_{fi} \rangle}{4 \sin 2\theta} \tag{10}$$

$$\langle -u'v' \rangle_{1F} = -\frac{\langle (B_{f2} - B_{f1})(B_{f4} - B_{f3}) \rangle}{4 \sin^2 \theta}. \tag{11}$$

While first-order full-spread homogeneity is a reasonable assumption for mean flows (which in this setting are a combination of regional scale currents, tidal currents and wind-driven currents, varying over length scales of many kilometres and minimum time scales of hours), it is by no means a uniformly safe assumption for turbulent flows, where even the largest eddies may have horizontal scales comparable to, or smaller than, half the beam spread. However in 1990, Lohrmann, Hackett & Roed proposed that two of the three turbulent shear stresses, specifically $\langle -u'w' \rangle$ and $\langle -v'w' \rangle$, could be estimated from radial current measurements made with a standard slant-beam ADCP, using the much weaker assumption that second-order statistics of the turbulent field are the same over the beam spread, i.e. that $\langle -u'w' \rangle_0 = \langle -u'w' \rangle_{\Delta} = \langle -u'w' \rangle_{-\Delta}$, $\langle u'u' \rangle_0 = \langle u'u' \rangle_{\Delta} = \langle u'u' \rangle_{-\Delta}$, etc., where the subscript denotes the horizontal location, relative to the centre of the beam array, at which the stress is determined. Subtracting time averages of (2–5) from the original equations, then squaring, yields equations for variances of the fluctuating part of the beam velocities. Using beam pair [1, 2] as an example

$$\langle B_{1f}^2 \rangle = \langle u'u' \rangle \sin^2 \theta + \langle w'w' \rangle \cos^2 \theta + \langle u'w' \rangle \sin 2\theta, \tag{12}$$

$$\langle B_{2f}^2 \rangle = \langle u'u' \rangle \sin^2 \theta + \langle w'w' \rangle \cos^2 \theta - \langle u'w' \rangle \sin 2\theta. \tag{13}$$

When the assumption of Lohrmann *et al.* which we term *second-order homogeneity* (subscript 2) is applied, (12) and (13), along with a similar set for the normal slant beam pair, can be used to estimate the two turbulent shear stresses

$$\langle -u'w' \rangle_2 = \frac{\langle B_{2f}^2 \rangle - \langle B_{1f}^2 \rangle}{2 \sin 2\theta} \tag{14}$$

$$\langle -v'w' \rangle_2 = \frac{\langle B_{4f}^2 \rangle - \langle B_{3f}^2 \rangle}{2 \sin 2\theta}. \tag{15}$$

A third set of expressions for these two shear stress components can be derived under an assumption of first-order half-spread (subscript $1H$) homogeneity which requires that the velocity field be homogeneous over only half the beam spread, such that $\langle B_{2f}(-\Delta, 0, z_i) w'(-\Delta, 0, z_i) \rangle = \langle B_{2f}(-\Delta, 0, z_i) w'(0, 0, z_i) \rangle$, etc. Then multiplying

Session	043			154		
f_{NY} (c.p.s.)	0.5208			0.4373		
Record	023	026	030	011	013	015
U_0^c (m s^{-1})	0.31	0.36	0.29	0.29	0.36	0.34
L_m (m)	30	35	28	033	41	39

TABLE 1. Values of the minimum horizontal spatial scale $L_m = U_0^c T$ retained by low-pass filtering with cutoff frequency $f_c = 0.02 f_{NY} = 1/T$. $U_0^c = ((U_1^c)^2 + (U_2^c)^2)^{1/2}$, where superscript '$c$' denotes mid-channel depth and values are averaged over record length. Values of U_1^c and U_2^c for these records may be found in table 3.

equations for B_{1f} and B_{2f} by $B_{5f} = -w'$ and averaging yields

$$\langle -u'w' \rangle_{1H} = \frac{\langle B_{f2} B_{f5} \rangle - \langle B_{f1} B_{f5} \rangle}{2 \sin\theta}, \tag{16}$$

and similarly,

$$\langle -v'w' \rangle_{1H} = \frac{\langle B_{f4} B_{f5} \rangle - \langle B_{f3} B_{f5} \rangle}{2 \sin\theta}, \tag{17}$$

These estimates should have twice the spatial resolution of the full-spread estimates.

For descriptions of the velocity fields associated with wind/wave-driven LC, the velocities first determined in instrument coordinates are subsequently rotated to 'wind coordinates' (x_1, x_2, x_3) where x_3 is vertically upwards from the bottom and x_1 and x_2 are, respectively, parallel to and 90° to the left of the record-averaged value of wind stress τ_s. In this coordinate system, the mean and fluctuating velocity components are $(U_1, U_2, 0)$ and (u_1', u_2', u_3'), respectively.

4.2. *Practice*

The open ocean measurements at LEO-15 present significant challenges to the use of the above techniques. First, surface wave velocities, which usually greatly exceed turbulent velocities, must be removed. Secondly, an appropriate 'mean' velocity must be determined and removed in order to derive 'turbulent' velocities: in a flow that varies with both wind and tide, definition of mean velocity is not straightforward. Finally, since we wish to determine all components of the turbulent velocity variances and shear stresses, the degree to which first-order full-spread homogeneity is achieved at the scales characteristic of LSC must be ascertained. These three challenges are addressed in the following.

4.2.1. *Removal of surface wave velocities*

Because of the wave-exposed nature of the observational site, the total velocity field is always dominated by velocities associated with surface waves. In strong storms, surface wave velocities reach $O(1\,\mathrm{m\,s^{-1}})$: even the minimum observed velocities, of $O(0.1\,\mathrm{m\,s^{-1}})$, are as large as, or larger than, expected turbulent velocities. However, turbulent structures are advected past the fixed VADCP at speeds characteristic of the mean flow, which fortunately is generally small, $O(0.3\,\mathrm{m\,s^{-1}})$ or less (see table 1). In contrast, surface waves pass at their phase speed, $c_p \sim 9$–$11\,\mathrm{m\,s^{-1}}$ for typical waves of 6–8 s period. This large difference in characteristic speeds separates the phenomena in frequency space. Figure 3 shows two representations of the power spectral density Φ_w of vertical velocity as a function of frequency f (c.p.s.): the Nyquist frequency $f_{NY} = 1/2T = 0.52$ c.p.s. is that of raw samples with $T = 0.96$ s. Nearly two decades

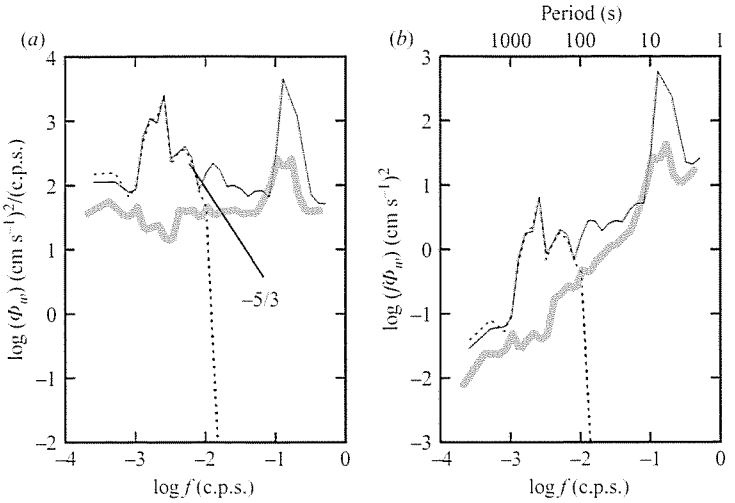

FIGURE 3. (*a*) Logarithmic and (*b*) variance-preserving spectra of vertical velocity w as a function of frequency: data is from a mid-water column bin of record 43.025. The raw spectra (solid line) of the original data, sampled at $1/0.96\,\mathrm{s} = 1.04\,\mathrm{c.p.s.}$, illustrate the separation of dominant surface wave periods (peak around 6–8 s period, $f = 0.13$–$0.17\,\mathrm{c.p.s.}$, $\omega = 0.8$–$1.0\,\mathrm{rad\,s^{-1}}$, at the right) and the much longer apparent periods associated with LSC (the low-frequency peak at the left). The separation in frequency of the two processes allows successful removal of surface wave velocities by low-pass filtering (dashed line). While the LSC signal is well above the level of a typical noise spectrum (grey curve), an inertial (−5/3) subrange that might be expected at higher frequencies cannot be resolved.

in frequency separate the large surface wave peak at the right from a broader low-frequency peak associated with the LSC structures. The dashed line in figure 3 is the result of application (forwards and backwards, to preserve phase) of a ninth-order Butterworth filter with cutoff frequency $f_c = 0.02\,f_{NY}$, followed by a [7 ping × 3 bin] neighbourhood average with Hanning weights in both dimensions. The result rolls off sharply at the point where the low-frequency signal falls to less than a decade above a typical noise spectrum (grey line) which in figure 3(*a*) is flat with frequency except for a surface wave peak at high frequency. Once the original data have been filtered, it is subsampled by a factor of ten, increasing the effective sample period to 9.6 s for most records used here.

Since measurements are time-based, the spatial scales remaining in the filtered data depend upon the speed at which they are advected past the fixed instrument. For a selection of records in the two episodes used in this paper, table 1 presents the smallest scales remaining in the filtered data, based on the speed $U_0^c = ((U_1^c)^2 + (U_2^c)^2)^{1/2}$, where superscript '*c*' denotes record-averaged values of downwind and crosswind velocities at mid-channel depth. For these cases, the scales retained are typically larger than ~30–40 m.

The time domain filtering used in this method of surface-wave removal requires a continuous data sequence, so can be applied only to data from acoustic bins that lie beneath the lowest instantaneous surface height during a record length. Both mean tidal height variation (up to ~2.5 m) and surface-wave displacements thus affect the extent of the water column that can be accessed with filtered data.

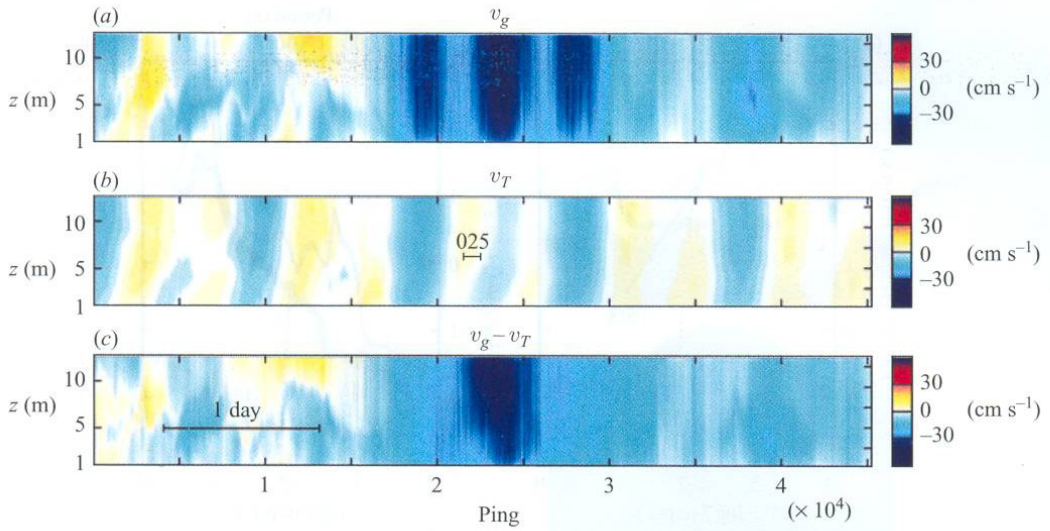

FIGURE 4. (*a*) North–south component v_g of the horizontal velocity field for Session 43, showing tidal modulation of the wind-driven current during the LSC event in the middle of the session. (*b*) North–south tidal component v_T determined by least-squares fitting to the five dominant tidal components at LEO-15 over the full session length. (*c*) North-south residual velocity field $v_g - v_T$.

4.2.2. *Definition of mean velocity*

In the laboratory or in a computer model, the concept of the mean velocity of a statistically stationary turbulent flow is straightforward: a mean velocity is derived by time-averaging over an appropriately long time, generally taken as at least several large-eddy time scales (Lenschow, Mann & Kristensen 1994). In the real world of the wind-forced tidally varying coastal ocean, an appropriate mean velocity is more difficult to define. In the absence of rotational effects, mean flow set up by a constant wind stress is strictly downwind. In reality, our measurements contain not only this downwind flow, varying over the typical storm time scale of a couple of days, but also possible rotational crosswind flows set up over a few inertial periods, and tidal flows varying in both speed and direction over the roughly 6 h period of the dominantly semi-diurnal tide in the region. Thus, in addition to determining an averaging period appropriate for separating 'turbulent' LSC structures, which appear with periods of several to tens of minutes, from a 'mean' flow varying on longer time scales, we must also decide what part of these more slowly varying flows should be considered as an appropriate mean flow for LSC. In particular, should the tidal component of the flow be (somehow) removed before determining a 'mean', or does an appropriate 'mean' include the tidal contribution?

It is clear that tides significantly modulate the mean flow within which LSC structures are embedded. Figure 4(*a*) shows north/south velocity component v_g over a period of 5 days that includes the LSC event shown in figure 2, clearly visible as the period of strongest velocity, between$\sim(1.7\text{–}3) \times 10^4$ pings. The obvious tidal-period modulation of the total velocity seen in figure 4(*a*) is greatly reduced (figure 4*c*) when the tidal velocity component v_T, shown in figure 4(*b*), is removed. (A tidal velocity component is determined by least-squares-fitting a horizontal component of the total velocity to complex sinusoids with periods of the five most significant tidal harmonics reported for tide stations bracketing the LEO-15 location, using the entire length of time available in a session. Fits are done independently for each bin.) Some

Session 043	024		025		026	
	(*a*)	(*b*)	(*a*)	(*b*)	(*a*)	(*b*)
$\langle u_1' u_1' \rangle_{x_3 t}$	12.9	12.7	13.4	12.6	10.7	9.5
$\langle u_2' u_2' \rangle_{x_3 t}$	10.3	10.2	15.9	9.5	14.7	7.7
$\langle u_3' u_3' \rangle_{x_3 t}$	2.6		3.4		2.0	
$\langle -u_1' u_2' \rangle_{x_3 t}$	1.1	0.92	4.5	2.3	3.6	0.76
$\langle -u_1' u_3' \rangle_{x_3 t}$	1.7	1.6	2.7	2.7	1.4	1.5
$\langle -u_2' u_3' \rangle_{x_3 t}$	−0.09	−0.00	−0.04	0.19	1.2	0.91

TABLE 2. Turbulent normal stresses (variances) and shear stresses in $(\mathrm{cm\,s^{-1}})^2$, averaged over depth and time for three LSC records from Session 43. See § 4.2.3 for the method of calculation of the components. Horizontal fluctuating (turbulent) fields are determined by removal of (*a*) the record mean or (*b*) a linear least-squares trend of horizontal velocity calculated separately for each bin. Vertical velocity variance, not affected by mean removal, is included to illustrate the magnitude relative to the horizontal variances.

of the features of the estimated tidal velocities agree with previously determined characteristics of shallow-water tides. In particular, the turn of the tide occurs first near the bottom and progresses upwards with time, speed increases upwards, and the diurnal inequality expected for this location is present. However, few of our sessions exceed 4–5 days in length, as a result of VADCP errors that accumulated when longer periods were attempted. Thus, the accuracy with which at least diurnal variations are represented by this fitting technique is in some doubt, while for some of the shorter sessions even the semi-diurnal tide may not be well represented (evidence for imperfect removal of a tidal component of the flow may be seen in the features remaining in figure 4(*c*) within the marker for one day). Removing tidal velocities fitted in this way, the only one available to us, would thus introduce unquantifiable uncertainty in a resulting 'mean' flow. Moreover, because the tidal fits are carried out over the entire session length, tide-removed velocity fields are available only for acoustic bins lying below the minimum height of the surface over the whole session, which further restricts the percentage of the water column available for analysis. Thus, we have chosen a more straightforward technique, basing our analyses on an individual record, with time extent less than a quarter of the dominant semi-diurnal tidal period. This period is large enough to encompass several LSC structures, allowing determination of statistically significant values for turbulent quantities (see § 5.1), but small enough that tidal variation appears as a nearly linear trend.

A fluctuating velocity component is thus defined by removal of a linear least-squares fit to the total measured velocity component over the record length (separately for each bin). The fitted tidal components discussed previously are not removed directly, although much of their effect will be removed indirectly with the linear trend. Dependence of results on the presence of residual tidal velocity is discussed where necessary. The degree to which the observations agree (as in many respects they do) with results from the purely wind-driven LES of Part 2 is probably due to the relatively small magnitude (figure 4*b*) of tidal velocities in the LEO-15 region, compared with those associated with wind-driven flows (figure 4*c*) during LSC episodes.

The importance of removing low-frequency variability, whether due to tides or wind is seen in table 2, which lists averaged values of components of the turbulent stresses

(in wind coordinates) for three LSC records from Session 43. (Averages are denoted by angle brackets rather than the more familiar overbar in order to avoid confusion with use of the latter for the average over resolved scales in the LES of Part 2. Added subscripts t and/or x_3 denote, respectively, averaging over the time extent of a record (~2.3 h) and/or over the vertical distance from the height above the bottom of the first measurement bin to the mimimum height at which sidelobe interference in slant beam measurements became possible: in profile plots, this height is denoted by a dashed line.) In a record such as 43.024 which has no visually obvious trend, comparison of values in columns (*a*) and (*b*) confirm that trend removal by linear least-squares fitting has little effect on any of the stresses. However, trend removal can result in significant reductions in either or both of the horizontal variances $\langle u_1' u_1' \rangle_{x_3 t}$ and $\langle u_2' u_2' \rangle_{x_3 t}$ and in the $\langle -u_1' u_2' \rangle_{x_3 t}$ stress component, as illustrated by the other two records which both have discernible variation of at least one component of the horizontal velocity field over the record length.

4.2.3. *Effect of beam spread*

Even with independent measurement of vertical velocity from a vertical beam, it is impossible to determine all six components (three normal stresses, or variances and three shear stresses) of the turbulent stress tensor without the assumption of first-order full-spread homogeneity for at least some of the components. Since we wish to use the full stress tensor in characterizing the observed flow structures, it is essential to determine the extent to which observed LSC satisfy this assumption.

Measurements in a wide variety of turbulent flows (Tennekes & Lumley 1972). show that the spatial scales that carry the shear stresses are smaller than those carrying the turbulent kinetic energy, whose components are the normal stresses. Thus, the shear stresses provide the most stringent test of first-order full-spread homogeneity. If estimates of shear stress components of LSC made under this assumption agree with those made under the weaker assumption of second-order homogeneity, we may have confidence that not only the shear stresses, but also the normal stresses, are not significantly affected by beam spread.

Figure 5 compares the two turbulent shear stress components $\langle -u_1' u_3' \rangle$ and $\langle -u_2' u_3' \rangle$ as calculated under assumptions of first-order full-spread, first-order half-spread and second-order homogeneity. Figure 5(*a*) shows stresses averaged in both height and time for a record containing LSC. All three stress estimates increase in magnitude with the number of samples averaged (M) until $M \sim 100$, corresponding to an averaging time interval of order ~16 min. This interval is thus a minimum averaging length required for stable stress estimates in these conditions, and is the same for all three estimates. Within the range of stable estimates (i.e. $M > 100$), stress magnitudes routinely increase from first-order full-spread, through first-order half-spread, to second-order estimates. However, all three estimates agree within their error bars, a result typical of record-averaged shear stresses during all episodes of LSC. When stresses are statistically different from zero, the maximum difference between the first-order full-spread and second-order estimates is ~20–25 %, differences between first-order half-spread and second-order estimates is ~3–5 % . Profiles of the record-averaged stresses (figure 5*b*) illustrate that agreement among the three stress estimates, within their standard deviation error bars, holds at all levels sampled, not just in the water column mean. Thus for the cases of full-depth Langmuir turbulence considered here, error in shear stresses is not dominated by error associated with spatial filtering by beam spread, even at the furthest range of the measurements, but rather by the

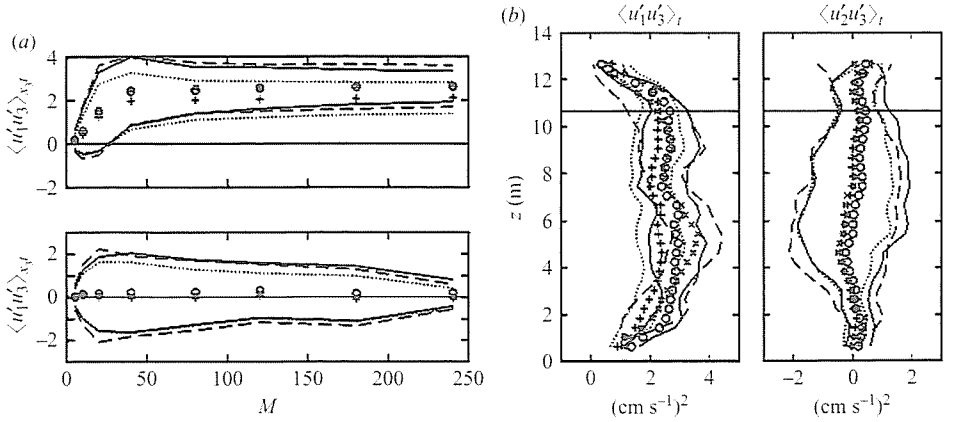

FIGURE 5. (*a*) Three estimates of turbulent shear stress components (in wind coordinates, averaged in time and height and their standard deviation error bars as functions of M, the number of samples in the estimate for a record (43.025) containing LSC. Estimates are calculated under assumptions of first-order full-spread homogeneity (+, dotted lines); first-order half-spread homogeneity (×, dashed lines); and second-order homogeneity (o, full lines). (*b*) Similar estimates of turbulent shear stress components and error bars, evaluated with $M = 180$ (~29 min), as functions of height z above the transducer: same symbols as (*a*). The dashed line marks the height above which slant beam sidelobe reflections from the surface could potentially contaminate the measurements.

relatively small number of large-eddy scales that are present in the time extent of one record.

The assumption that normal stresses would be equally well determined, since they reside at similar or larger scales, was investigated by comparing various slant beam representations of vertical velocity variance $\langle u_3'u_3'\rangle$ with that supplied by the vertical beam. Vertical velocity value estimated as w_{1F} (using all four slant beams, (8)) was ~75 % of the true value throughout the measured water column, rising to ~90 % at ~2 m above the bottom, whereas single slant beam pairs gave estimates that ranged from 75 % to 95 % of the true value. We have no explanation for the lack of degradation of performance with increasing height (beam spread) that is observed, nor for the irregular nature of the improvement of single-pair estimates relative to the four-beam average: both may result from the highly anisotropic nature of the underlying flow structures. Nonetheless, for the LSC records being considered, the accuracy with which at least the vertical velocity variance is determined by a first-order full-spread estimate is comparable to that of the determination of the full-spread estimates of the two shear stresses discussed above. The estimates of the horizontal velocity variance and the $\langle -u_1'u_2'\rangle$ shear stress should involve the same degree of error due to beam spread effects, namely an underestimation by ~25 %. (With colleagues Tejada-Martínez & Grosch (Part 2), we are in the process of producing an estimate of the Doppler 'response' function by sampling 'flow' produced by an LES with the appropriate geometry. Preliminary results using a Langmuir-forced LES generally confirm the conclusions reached here.) In what follows (and in table 2), we use the (most accurate) vertical beam estimate for $\langle u_3'u_3'\rangle$, the first-order full-spread estimates for $\langle -u_1'u_2'\rangle$, $\langle u_1'u_1'\rangle$ and $\langle u_2'u_2'\rangle$, and first-order half-spread estimates (of intermediate accuracy) for $\langle -u_1'u_3'\rangle$ and $\langle -u_2'u_3'\rangle$. Results are qualitatively similar if all six stress components are determined from full-spread estimates.

5. Observed characteristics of Langmuir supercells

This section illustrates various characteristics of fluctuating velocity fields observed during periods of extended strong wind/wave forcing, characteristics that lead to identification of the underlying features as Langmuir circulations extending through the full depth of the water column.

First however, we examine values of two dimensionless parameters, the turbulent Langmuir number La_t and the buoyancy Langmuir number La_b, that have been defined to gauge the magnitude of C-L vortex forcing relative to forcing by surface wind stress and surface buoyancy flux, respectively. As defined by McWilliams *et al.* (1997), the turbulent Langmuir number $La_t \equiv (u_\tau/u_s)^{1/2}$ involves the ratio of the friction velocity $u_\tau = (\tau_s/\rho_0)^{1/2}$, where τ_s is surface wind stress magnitude and ρ_0 water density, to the surface Stokes drift velocity u_s. For $La_t < 1$, turbulence caused by C-L vortex forcing is expected to dominate that associated with wind stress. The buoyancy Langmuir number $La_b \equiv (4B_0/\beta u_s u_\tau^2)$, where B_0 is the surface buoyancy flux and $\beta = 1/|2\kappa|$ is the e-folding depth of the Stokes drift, was originally defined by Li & Garrett (1995):† $La_b \ll 1$ implies the insignificance of forcing by (unstable) buoyancy flux relative to the C-L vortex force. While both B_0 and u_τ are readily calculated from the observed meteorological fields, determination of appropriate values of u_s and β is less straightforward. First, the observational surface wave field is not that of a monochromatic wave. Moreover surface waves at LEO-15 are neither deep-water nor shallow-water waves. Instead, with dominant wavelengths of the order of 5–6 times the mean water depth (see below), these are waves in water of intermediate depth, intermediate waves for brevity.

To proceed, available information was used to determine the amplitude a, frequency $\omega = (g\kappa \tanh \kappa H)^{1/2}$ and horizontal wavenumber κ of a representative monochromatic intermediate surface wave. Taking record 43.025 as an example, frequency $\omega = 0.82\,\mathrm{rad\,s^{-1}}$ is determined from the high-frequency surface wave peak of the spectrum of total vertical velocity (see figure 3), and an associated value of $\kappa = 0.08\,\mathrm{rad\,m^{-1}}$ (corresponding to wavelength $\Lambda = 79\,\mathrm{m}$, hence $\Lambda/\mathrm{H} \sim 5$) is derived from the intermediate wave dispersion relationship with $H = 15\,\mathrm{m}$. In deciding on an appropriate amplitude, two available metrics were considered. First, the coarsely resolved surface height field provided by tracking the surface in the vertical beam backscatter field yields a value of r.m.s. $\zeta = 0.6\,\mathrm{m}$ for r.m.s. wave amplitude, hence $a \sim 0.8\,\mathrm{m}$. When derived from bottom pressure r.m.s. $\zeta = 0.28\,\mathrm{m}$, hence $\zeta \sim 0.4\,\mathrm{m}$. Correcting this value for depth-dependence of pressure under intermediate waves provides an estimate of $a \sim 0.7\,\mathrm{m}$, reasonably close to the result of the first technique. Thus, an appropriate amplitude to characterize a monochromatic representation of the true wave field appears to be in the range $a = 0.7$–$0.8\,\mathrm{m}$.

When calculated with $u_s = \omega\kappa a^2 \coth(\kappa H)$, the surface Stokes drift magnitude for intermediate waves, using the above values of a, ω and κ and observed values of B_0, τ_s and H, $La_b = 0.004$ and $La_t = 0.48$ for record 43.025. For sets of multiple records used later, values calculated with wave amplitudes estimated from corrected bottom pressure are in the ranges $0.003 < La_b < 0.01$, $0.5 < La_t < 0.7$ for 43.023–43.030 and $0.006 < La_b < 0.01$, $0.6 < La_t < 0.8$ for 154.011–154.015. Low values of La_b imply dominance of Langmuir forcing over unstable buoyancy forcing (Li *et al.* 2005) in

† Li & Garrett (1995) originally named this ratio *Ho*, the Hoenikker number, after a character (apparently modelled after Irving Langmuir) in Kurt Vonnegut's novel *Cat's Cradle*. An extremely determined reviewer has forced us to rename this ratio in a more traditional fashion.

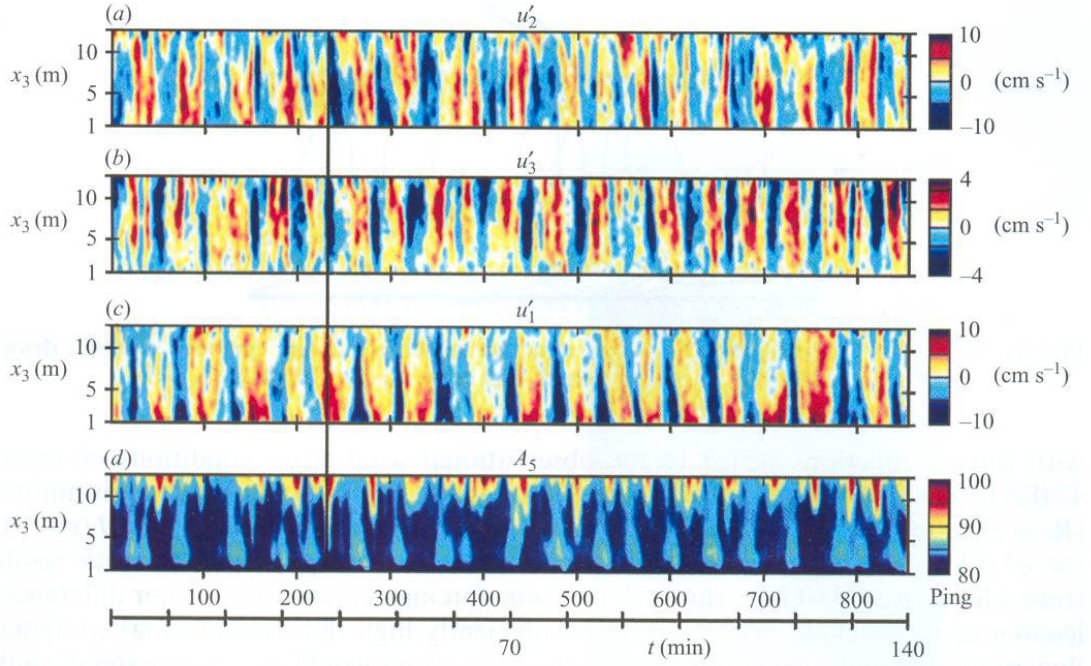

FIGURE 6. Depth/time sections of fluctuating (*a*) crosswind velocity u_2', (*b*) vertical velocity u_3' (*c*) downwind velocity u_1', and (*d*) vertical beam backscatter amplitude A_5 for a record (43.025) within the LSC episode shown in figure 2. The sampling period is 9.6 s: the total record length is ~ 2.3 h. As described in § 4.2.2, the fluctuating velocity field is that left after a linear least-squares fit at each bin has removed a slowly varying 'mean' velocity associated with a combined wind and tidally forced flow. The vertical line draws attention to synchronous features mentioned in the text.

both sets of records. Values of La_t are larger than those typically quoted as assuring dominance of Langmuir forcing in the deepwater case (McWilliams *et al.* 1997; Li *et al.* 2005), and at first glance might be interpreted as implying weak Langmuir forcing. However, the C-L vortex force, as formulated by Craik & Leibovich (1976), is not only inversely proportional to the square of the Langmuir number, but also directly proportional to a function $\phi_1^s(\kappa, d)$ (where d is the distance beneath the surface) that expresses the decay of the Stokes drift with depth. Thus, La_t is not a unique scale for the strength of Langmuir forcing: it is also necessary to specify surface wave character. Previous observations and LES have been for deep-water surface waves where ϕ_1^s decays exponentially with depth; in such cases, it has been observed that the Langmuir number has to be of order 0.3 to 0.4 for Langmuir turbulence to dominate the dynamics. For the intermediate surface wave observations reported here, ϕ_1^s decays more slowly with depth (see (2.4), Part 2) than do deep-water waves. This slower decay offsets the somewhat larger values of observed La_t, resulting in Langmuir turbulence being dominant in the accompanying LES (Part 2) and in our observations at these higher turbulent Langmuir numbers.

In the following examination of LSC, we use records taken primarily from the springtime episode (Session 43) documented in figure 2: however, records from another episode (Session 154) among several that occurred in the autumn are added to illustrate that the features shown are characteristic of other realizations of this phenomenon. Throughout descriptions of flow features, comparisons will be made with the results of LES runs in Part 2 that treat the case of intermediate surface waves

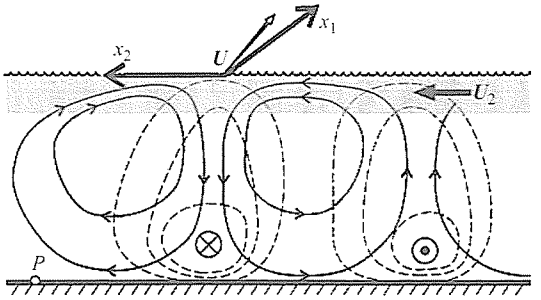

FIGURE 7. Features of the cellular velocity structure observed during episodes of LSC: drawn for record 43.025 (figure 6) which has crosswind mean flow $U_2 > 0$.

with forcing functions scaled to the observational wind/wave conditions of record 43.025 ($La_t \sim 0.4$) and 154.14 ($La_t \sim 0.7$). The highest computational Reynolds number ($Re = 395$) does not come close to that of the observations, typically $Re = w'H/\nu \sim 10^5$ for $w' \sim 1\,\mathrm{cm\,s^{-1}}$, $H \sim 15\,\mathrm{m}$ and $\nu \sim 10^{-2}\,\mathrm{cm^2\,s^{-1}}$. However, comparison with results from a lower $Re = 180$ LES run with the same forcings, reveals only minor differences, leading us to conclude that $Re = 395$ is sufficiently high that fundamental computed flow properties and their comparison with observations would not change significantly with further increase in computational Re.

5.1. *The three-dimensional velocity field*

For the investigation of Langmuir circulations and comparison with LES results, the three-dimensional fluctuating velocity field is transformed from instrument-based coordinates to the 'wind' coordinates (x_1, x_2, x_3) described in § 4.1. This transformation is an appropriate one provided (i) the wind direction measured at the tower is the same as that at the measurement site, (ii) wind direction remains approximately constant over a record length, (iii) Langmuir cells exist with the expected morphology, i.e. structures elongated in one horizontal direction, and (iv) that they are lined up with this long dimension at least roughly downwind. The first assumption is a reasonable one, given unobstructed marine fetch between the node location and the meteorological tower in the northeasterly winds associated with LSC episodes, as well as the results of Münchow & Chant (2000) referred to earlier. A specific illustration of the general validity of the second assumption during LSC events is provided by figure 2(*b*). In the following section, we show how the fourth assumption explains many of the characteristic features of the observed velocity and backscatter fields. In § 6, we show that the third assumption provides the simplest explanation of observed variability in the apparent period of large-eddy fluctuations as observed by the fixed VADCP. Accepting all four assumptions for now, a realization of the three-dimensional velocity field in wind coordinates is shown in figure 6, together with the vertical beam backscatter amplitude. To aid the following discussion of features that agree with those considered typical of Langmuir circulations, as well as some that are singular to this shallow regime where LC fill the water column, figure 7 shows significant features of the observed cells.

Regions of strong downward vertical velocities (blue-coded, figure 6*b*) are highly correlated with regions of strong backscatter that originate from the surface (figure 6*d*). Such backscatter signatures have been widely interpreted as the signature of air microbubbles injected near the surface by surface wave breaking and advected to depth in the downwelling limbs of Langmuir circulations (Zedel & Farmer 1991).

The downwelling limbs are separated by upwelling zones (red-coded, figure 7*b*) that are highly correlated with clouds of high backscatter originating from the bottom, a feature not formerly observed, but here always seen in connection with the characteristic velocity structures shown in figure 6. We interpret these clouds as being due to scattering from sediment and/or bioactive material that, having been resuspended in a highly sheared but thin surface-wave bottom boundary layer (Trowbridge & Agrawal 1995), is being moved through the full extent of the water column in the upwelling limbs of Langmuir circulations that fill the entire water column.

A field of statistically stationary LSC will appear as fluctuating velocities observed at a point only if they are being advected past the point: since LC have larger variability in the crosswind than the downwind direction, perceived variability will come mainly as a result of crosswind advection. For the record shown in figure 6, mean crosswind velocity $U_2 > 0$ (see table 4), so crosswind drift of cells past a fixed point P on the bottom is towards the left in figure 7. As a downwelling region approaches P, the horizontal cross-wind component (u_2', in direction x_2) near the bottom should first be positive, then switch to negative at the centre of the downwelling, a relationship clearly observed between u_2' and u_3' in figure 6(*a*, *b*). The observed field of u_2' does not show horizontal flows near the surface that are out of phase with those observed at depth, apparently because the upper 20 % of the mean water column could not be sampled during this period of large surface waves. However, absence of the necessary near-surface convergent/divergent flows within the sampled domain implies that the actual horizontal crosswind flows are indeed strongly surface-intensified, as illustrated in figure 7 (and in Pollard (1976) who apparently based this particular feature on some of Langmuir's original observations using subsurface drifters made from umbrellas). Surface-intensification is also implied in the deep-water observations of Weller & Price (1988), who reported increasing vertical shear of horizontal velocity as the surface was approached.

As found in previous observational studies (Langmuir 1938; Smith *et al.* 1987; Weller & Price 1988), downwind 'jets' (red-coded, figure 6*c*) are located over the downwelling regions, compensated by regions of slower than average downwind flow beneath the upwelling regions. Unlike previous deep-water observations, the jets are strongly bottom-intensified in this shallow-water intermediate wave regime, in agreement with similarly configured LES with Langmuir forcing (Part 2). In this record, the zero isotachs of the downwind velocity component u_1' are observed to lean to the left with increasing height above the bottom, suggesting 'tilted' cells. However, an actual physical tilt of the cells in the crosswind plane would necessarily also appear in the other velocity components. Since zero isotachs of both u_3' and u_2' are vertical, the apparent inclination of the u_1'-component should be interpreted as a phase lag as the bottom is approached, rather than an actual tilt of the cells. Whatever its cause, the structure of such a phase lag of u_1' relative to u_2' will result in the positive values of $\langle -u_1'u_2' \rangle$ that are observed in this record (see figure 9). However, the phase lag is not a consistent feature of the LSC records; while many records exhibit a lag like that seen in figure 6, many others do not (although it should be noted that no record consistently shows the opposite phase lag). Since no such phase lag appears in the LES results, it must result from a mechanism not incorporated in the LES physics, moreover a mechanism present only sporadically in the observational setting.

Maximum downwards vertical velocities occur at depths at or above mid-depth, as shown in figure 8 for a selection of records. In each set of panels, variables

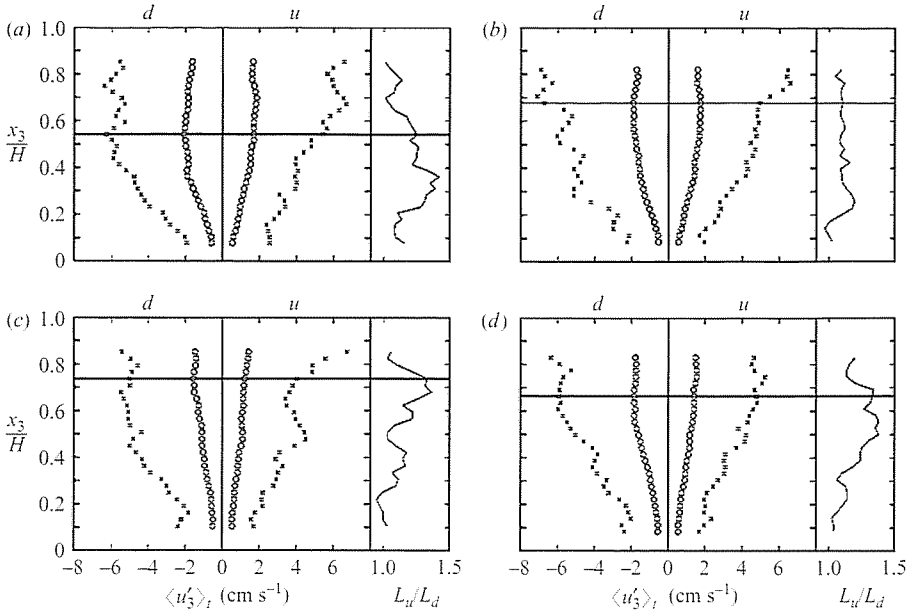

FIGURE 8. The left-hand plots of each panel show profiles, as functions of height above bottom x_3 normalized by record-mean water column height H, of (o) downwards (d) and upwards (u) time-averaged vertical velocities $\langle u'_3 \rangle_t$ observed in four different records containing LSC. Crosses indicate the extreme values present in each bin, and the horizontal line in each panel is the vertical location of the maximum value of $\langle |u'_{3d}| \rangle_t$. Right-hand plots are profiles of the ratio of the horizontal extent of upwelling to downwelling regions, determined as $L_u/L_d \sim \langle |u'_{3d}| \rangle_t / \langle u'_{3u} \rangle_t$. All records have maximum average downwards vertical velocity above mid-depth, and tend to have $L_u/L_d \geqslant 1$ throughout the profile, both features considered characteristic of LC. Maximum values of instantaneous $|u'_{3d}|$ at the depth of maximum $\langle |u'_{3d}| \rangle_t$, and 10 m wind speeds U_{10} averaged over the record length are: (a) 43.025: $|u'_{3d}| = 6.3\,\mathrm{cm\,s^{-1}}$, $U_{10} = 8.6\,\mathrm{m\,s^{-1}}$ (b) 43.023: $|u'_{3d}| = 6.7\,\mathrm{cm\,s^{-1}}$, $U_{10} = 7.8\,\mathrm{m\,s^{-1}}$, ($c$) 154.013: $|u'_{3d}| = 5.0\,\mathrm{cm\,s^{-1}}$, $U_{10} = 10.6\,\mathrm{m\,s^{-1}}$, ($d$) 043.029: $|u'_{3d}| = 5.9\,\mathrm{cm\,s^{-1}}$, $U_{10} = 8.8\,\mathrm{m\,s^{-1}}$.

conditionally averaged in time over the record length are shown as functions of height above bottom x_3 normalized by H, record mean water column depth. The left-hand profiles are of negative and positive vertical velocities, averaged separately (circles); crosses indicate the largest negative and positive magnitudes of u'_3 observed at each depth. The depth below mean surface of maximum average downwards vertical velocity is $d_m \sim (0.3\text{–}0.5)H$ in these observations. Open ocean measurements of Smith *et al.* (1987) suggested $d_m \sim 0.5H$, where H is surface mixed layer depth, while those of D'Asaro (2001) found $d_m \sim 0.2H$ (although D'Asaro's value may be an underestimate, since he uses the observed surface mixed-layer depth, generally larger than the depth of active mixing as revealed by neutrally buoyant float trajectories, for the scale H). The LES of Part 2 yield values of $d_m \sim (0.4\text{–}0.5)H$, slightly deeper than our observations and considerably deeper than the values of $d_m \sim (0.1\text{–}0.2)H$ obtained by McWilliams *et al.* (1997). The difference between the two LES results is argued to result from the difference in the character of surface waves responsible for the Langmuir vortex forcing in the two settings (i.e. intermediate waves in the present case, deep-water waves in the McWilliams *et al.* LES), as well as differences in bottom boundary conditions.

On the right-hand side of each panel in figure 8 are profiles of the ratio $\langle |u'_{3d}| \rangle_t / \langle u'_{3u} \rangle_t$ which, through mass continuity, must be of the same order as a horizontal asymmetry

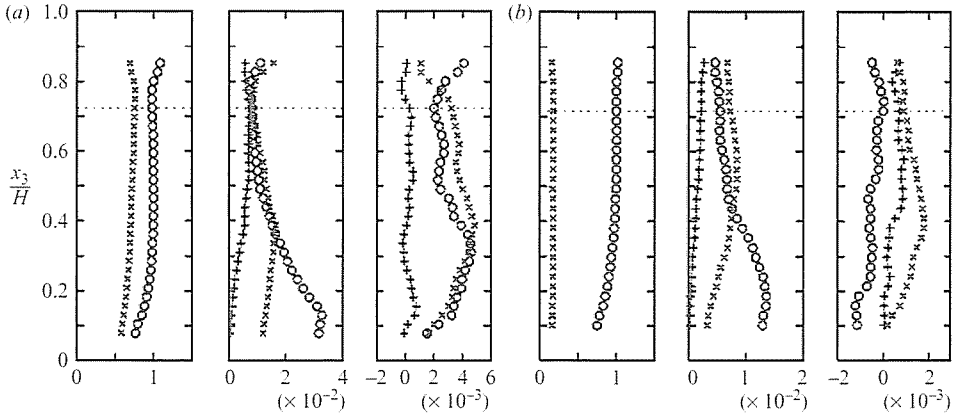

FIGURE 9. Profiles of mean and turbulent quantities normalized by U_1^c, mean downwind speed at mid-channel as functions of height above bottom x_3 normalized by H, mean water column height over the record length. The dashed line denotes height above which horizontal velocity estimates may possibly be affected by sidelobe reflections from the surface. In each set: left-hand panel: mean downwind (o, U_1^n) and crosswind ($\times$, U_2^n) velocities; centre panel: normal stresses (o, $\langle u_1' u_1' \rangle_t^n$, $\times$, $\langle u_2' u_2' \rangle_t^n$, +, $\langle u_3' u_3' \rangle_t^n$); right-hand panel: shear stresses ($\times$, $\langle -u_1' u_3' \rangle_t^n$, +, $\langle -u_2' u_3' \rangle_t^n$, o, $\langle -u_1' u_2' \rangle_t^n$), time-averaged over record length. (*a*) Record 43.025: $U_1^c = 27\,\mathrm{cm\,s^{-1}}$, $La_t = 0.48$, $La_b = 0.004$ (*b*) Record 154.014: $U_1^c = 37\,\mathrm{cm\,s^{-1}}$, $La_t = 0.72$, $La_b = 0.006$.

ratio $r = L_u/L_d$ determined by the horizontal widths of the upwelling and downwelling regions L_u and L_d, respectively. Because observed downwelling velocities tend to be larger in magnitude than upwelling velocities, r is characteristically greater than one throughout the profiles, i.e. downwelling regions are narrower than upwelling regions. For the records shown in figure 8, ratios calculated at $x_3/H = 0.5$ range from 1.1 to 1.4. Similar values from the LES of Part 2, vary somewhat with La_t: runs with $La_t = 0.7$ have $r \sim 1.5$ at mid-depth, whereas r approaches unity for $La_t = 0.4$. The ranges of values from both observations and the accompanying LES are in general agreement with other computational estimates (Skyllingstad & Denbo 1995; McWilliams *et al.* 1997).

Maximum instantaneous downwards vertical velocity at these same depths (i.e. those of the horizontal lines in figure 8) are given in the figure caption, along with record-averaged values of U_{10}, the wind speed measured at 10 m height. The observed maxima of $|u_{3d}'|$ lie in the range 5.0–6.7 $\mathrm{cm\,s^{-1}}$, in rough agreement with values of 6.2–8.5 $\mathrm{cm\,s^{-1}}$ predicted from the formula $|u_{3d}'| = 0.008 U_{10}$ derived by Li & Garrett (1997) for a fully developed surface wave field (see also Leibovich 1983). In detail however, the largest predicted value does not correspond to the largest wind speed, suggesting an additional (but in these conditions, relatively minor) dependence on details of wind and/or surface wave fields.

5.2. *Vertical profiles*

Figure 9 presents profiles of various mean and turbulent quantities in wind coordinates for individual LSC records from two different sessions. (As discussed in §4.2.2, problems associated with slowly varying mean flow conditions are reintroduced by extending the averaging length, so the profiles shown here are based on averages over a single record. Despite relatively large error bars associated with the stochastic nature of the turbulent flow, individual shear stress components are observed to differ significantly from zero.) All quantities, plotted as functions of height above bottom

	(a)	(b)
$\langle u_1' u_1' \rangle^n_{x_3 t}$	0.016	0.015 ± 0.0085
$\langle u_2' u_2' \rangle^n_{x_3 t}$	0.013	0.013 ± 0.0030
$\langle u_3' u_3' \rangle^n_{x_3 t}$	0.0049	0.0047 ± 0.0020
$\langle -u_1' u_2' \rangle^n_{x_3 t}$	0.0031	0.0033 ± 0.0029
$\langle -u_1' u_3' \rangle^n_{x_3 t}$	0.0034	0.0033 ± 0.0014
$\langle -u_2' u_3' \rangle^n_{x_3 t}$	0.0002	0.0003 ± 0.00078

TABLE 3. Values of turbulent stress components, normalized (superscript n) by downwind velocity $U_1^c = 27\,\mathrm{cm\,s^{-1}}$ at mid-depth in the water column, for record 43.025. Subscript x_3 indicates averaging over all available bins in the vertical. Subscript t indicates averaging over (*a*) the entire record (873 samples) or (*b*) three consecutive lengths of 240 samples each within the record: in the latter case, the small-sample standard deviation is also available.

x_3 normalized by H, record mean water height, are normalized (superscript n) by the appropriate power of U_1^c, downwind speed at mid-depth in the channel. (Alternative choices for scaling velocity were considered but rejected. The mean flow profile did not exhibit a logarithmic layer near the bottom, so the bottom friction velocity was not a relevant scaling velocity (nor, given the lack of a log layer, did we have a means of determining it). In a wind-wave driven flow, it is not clear *a priori* which of u_τ, the friction velocity associated with surface wind stress, or u_s, the surface Stokes drift, would be an appropriate scaling velocity. U_1^c is chosen as the scaling velocity because it is a flow-related variable readily determined both in the LES study of Part 2 and from the observations (the time- and depth-averaged downwind velocity $\langle U_1 \rangle_{x_3 t}$, more usual for LES studies, is observationally inaccessible as a result of loss of data near the surface through the filtering process used to remove surface wave velocities). Wind and surface wave characteristics remained reasonably steady during the two records seen in figure 9. In each part of the figure, left-hand panels show mean downwind and crosswind velocity components, followed by normal stresses (or variances, centre panels) and shear stresses (right-hand panels): values shown are time averages (subscript t) over the record length.

With the number of variables profiled in figure 9, error bars have been omitted for clarity. An appreciation of the size of error bars (due to the relatively small number of large eddies present in a single record) in profile plots may be gained from figure 5(*b*), which shows error bars associated with two of the shear stresses of record 43.025. Another indication of the variability involved is obtained by comparing depth-averages of the normalized time-averaged stresses seen in figure 9 with the values and small-sample standard deviations obtained by using three $M = 240$ values contained within a record. As illustrated in table 3 for record 43.025, the two methods yield mean values of all components that agree within the standard deviation provided by the second method. Standard deviations of the shear stresses indicate that $\langle -u_2' u_3' \rangle^n_{x_3 t}$ is not significantly different from zero, $\langle -u_1' u_3' \rangle^n_{x_3 t}$ is significantly different from zero, and $\langle -u_1' u_2' \rangle^n_{x_3 t}$ is only marginally so.

A broader view of the statistical significance of the measured turbulent stresses is obtained by selecting periods of roughly constant wind/wave forcing and considering successive records within these periods as individual realizations of the turbulent flow. Figure 10 shows ensemble mean (denoted by addition of superscript '*e*') normalized stress profiles, with small-sample standard deviation error bars, for two such periods

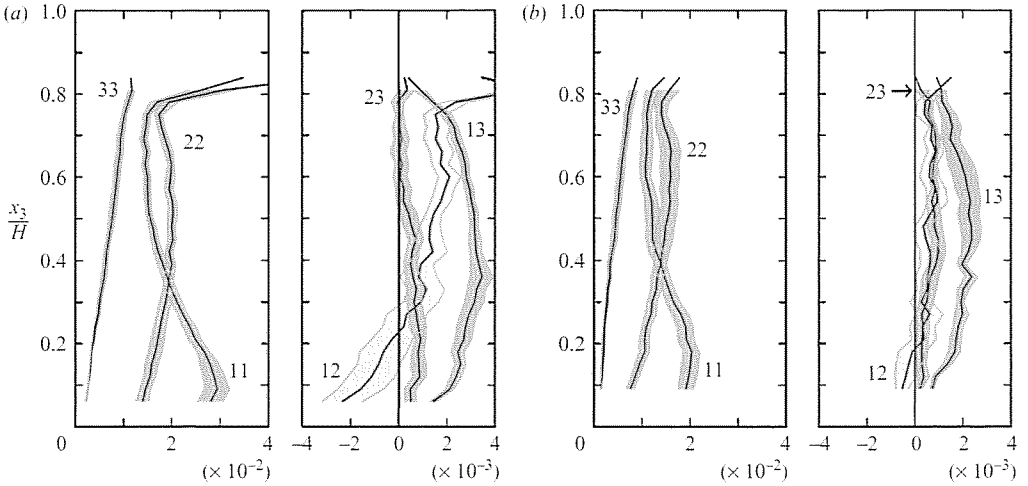

FIGURE 10. Profiles of ensemble-averaged normal (right-hand sides) and shear (left-hand sides) stress components and one standard deviation error bars for ensembles consisting of (*a*) eight records (023–030) from Session 43 and (*b*) five records (011–015) from Session 154. Labels $ii = \langle u_i' u_i' \rangle_t^{ne}$, $ij = \langle -u_i' u_j' \rangle_t^{ne}$.

containing, respectively, eight and five records. Mean wind speed and direction lie within 7.8–8.8 m s^{-1}, 230–246° for a late spring period (figure 10*a*) that includes record 43.025 (figure 9*a*), and within 8.4–11.0 m s^{-1}, 216°–222° for an early autumn episode (figure 10*b*) that includes record 154.014 (figure 9*b*). While the general shapes of all the stress component profiles agree between the two episodes, the scaled magnitudes generally do not agree within the error bars. The difference between the two ensembles is what would arise if U_1^c were underestimated by ~ 15–20 % on average for episode (*a*) or, alternatively, overestimated by the same amount for episode (*b*). These alternative possibilities are explored by comparing record-averaged total velocity components at mid-depth with similar values computed after removal of tidal velocities estimated over each episode. (For reasons elaborated in § 4.2.2, we do not use the tidal estimates made by our fitting techniques to define the fluctuating turbulent fields. However, the fitted tides provide estimates of the magnitude and direction of the tidal contribution which should be sufficiently accurate to assess at least the direction of change in U_1^c for a given record.) For the weak tides (surface height variation ~ 1.5 m) that characterize episode (*b*), inaccuracy of a tidal fit should be less important than it will be for the stronger tidal flows (surface height variation ~2.5 m) at the time of episode (*a*). As seen in table 4, for all records of Session 154, tidal removal has a minor effect on downwind mean flow, while effectively reducing crosswind mean flow to zero. We thus conclude that for this session (figure 10*b*), the observed crosswind flow is associated with the tides and the U_1^c-scaled profiles would be little affected by tidal removal. In contrast, table 4 indicates that for many of the records in Session 43, the value of U_1^c used to scale the profiles is substantially underestimated owing to partial cancellation of the wind-driven flow by an adverse tidal flow (see figure 4). Because of uncertainty as to the accuracy of the tidal fitting technique, we have not carried out a renormalization of the profiles in figure 10(*a*) based on the values of $U_1^{cT} > U_1^c$ in table 2. However, it is clear that such renormalization would, in general, move the profiles towards the smaller normalized values seen in figure 10(*b*). We conclude that the magnitudes of the normalized turbulent stresses in figure 10(*a*) are probably

43	U_1^c	U_1^{cT}	change (%)	U_2^c	U_2^{cT}	Change (%)	154	U_1^c	U_1^{cT}	change (%)	U_2^c	U_2^{cT}	change (%)
023	26	24	−9	17	15	−10	011	26	30	+13	12	2	−80
024	28	28	−2	13	16	+24	012	30	32	+6	15	3	−83
025	27	35	+28	19	18	−1	013	34	33	−1	13	4	−73
026	24	38	+60	26	17	−37	014	37	36	−3	6	2	−65
027	27	39	+47	26	14	−47	015	34	35	−1	1	−1	−200
028	27	33	+20	17	12	−29							
029	29	28	−2	9	10	+9							
030	28	25	−12	10	7	−29							

TABLE 4. Sessions 43 and 154, mid-depth record-averaged mean velocity components ($\mathrm{cm\,s^{-1}}$) in wind coordinates before (superscript 'c') and after (superscript 'cT') removal of fitted tidal components (§4.2.2), and percentage change. $\{U_1^c, U_2^c\}$ are, respectively, downwind and crosswind components at $H/2$, where H is record-average depth.

overestimates as a result of underestimation of U_1^c, and that the results shown in figure 10(*b*) are quantitatively the more reliable, since little affected by tidal removal.

While removal of fitted tides moves the cross-wind velocity U_2^c towards zero in Session 43, (table 4), substantial residual crosswind flow remains. The magnitude of this residual flow seems too large to attribute totally to inaccuracy of the tidal fitting procedure at this period of stronger tides. Moreover with tides removed, the overall mean flow has a strikingly consistent geographic direction (211°–219° for records 43.023–030) which roughly parallels the nearby shoreline. One possible explanation is that the residual flow represents the annual 'mean' flow, which is roughly southwestward at LEO-15. However, as described by Kohut *et al.* (2004), the annual mean flow is not only smaller (maximum $\sim 10\,\mathrm{cm\,s^{-1}}$) than the maximum observed residual mean flow, but should be, by definition, stationary in time. In contrast, the observed residual flow in Session 43 varies with time. It thus seems possible that the residual mean flow is a geostrophic component parallel to the coast, the result of an offshore pressure gradient set up by Ekman transport towards the coast. Since the strike of the shoreline is to the left-hand side of the wind direction during Session 43, such a pressure-driven component parallel to the coast would explain values of residual U_2^{cr} that are consistently positive (table 4), i.e. to the left-hand side of the wind, rather than to its right as would be expected for rotationally influenced flows in an unbounded domain. Absence of a significant along-coast component in Session 154 may be a function of extended wind history. While winds blew from the north or northwest for the 2–3 days preceding the nor'easter of Session 43, antecedent winds for that of Session 154 were upwelling winds from the southeast, associated with set-down, rather than set-up, at the coast. We conclude that the observed total crosswind velocity certainly has a tidal component, but may also (dependent upon wind forcing history) have a significant component arising from rotational effects in the presence of a nearby lateral boundary. The action of rotation in the presence of this boundary is a significant difference from the horizontally homogenous LES without rotation carried out in Part 2. However, previous LES studies (McWilliams *et al.* 1997; Li *et al.* 2005) indicate that rotation affects mean velocity profiles, but has little effect on turbulence statistics. We thus proceed to compare our observations of turbulence statistics with results of the LES of Part 2.

Examining the ensemble-averaged stress profiles of Session 154 (which we have argued are the most quantitatively reliable), we find general agreement with the

shapes and relative magnitudes of the stress component profiles from the associated Langmuir-forced LES for intermediate surface waves ($\lambda = 6H$) and turbulent Langmuir numbers between 0.4 and 0.7. For the latter case, we use computational results at $Re = 395$, for the former results at $Re = 180$: Part 2 demonstrates only slight differences between results for different Re at the same La_t. The observed vertical velocity variance $\langle u_3' u_3' \rangle_t^n$ has a maximum that is not resolved in figure 10(*b*): we can only conclude that the maximum non-dimensional magnitude is $\geqslant 0.01$ at depths $x_3/H > 0.8$. The LES of Part 2 show this maximum increasing in magnitude and moving upwards from mid-channel with decrease in La_t, from magnitude ~ 0.005 at $x_3/H \sim 0.5$ for $La_t = 0.7$ to magnitude ~ 0.01 at $x_3/H \sim 0.7$ for $La_t = 0.4$. Thus, the observations agree best with LES results with the lower value of La_t. In agreement with the LES, observed downwind variance $\langle u_1' u_1' \rangle_t^n$ has a near-bottom maximum, although its normalized magnitude is somewhat smaller. Observed crosswind variance $\langle u_2' u_2' \rangle_t^n$ is smaller than downwind variance near the bottom, but increases to equal and subsequently exceed it at a height of $x_3/H \sim 0.4$. In the LES of Part 2, this height decreases with La_t, from $x_3/H \sim 0.7$ for $La_t = 0.7$ to only $x_3/H \sim 0.2$ for $La_t = 0.4$: the value observed again suggests that the observations are best described by $La_t = 0.4$. As in the associated LES, the observed $\langle -u_1' u_3' \rangle_t^n$ shear stress is positive and relatively uniform with height in the interior of the water column, though with a somewhat smaller magnitude.

The LES results indicate that the major contrast in the vertical stress profiles between Langmuir and Couette cases is associated with increase in the crosswind flow component away from the bottom boundary, so that $\langle u_2' u_2' \rangle \sim \langle u_1' u_1' \rangle$ in the Langmuir case rather than $\langle u_2' u_2' \rangle \ll \langle u_1' u_1' \rangle$ characteristic of Couette flow. The observations show the former, reinforcing interpretation of the measurements as LC. Overall, the observations of Session 154 agree best with simulations for $La_t = 0.4$, suggesting that the present method of estimating La_t from properties of a dominant surface wave needs improvement, which will be possible only with more detailed information about the surface wave spectrum.

Despite the agreement between various ensemble-averaged observational fields and LES results discussed above, there remain significant discrepancies. First, although $\langle -u_2' u_3' \rangle_t^{ne}$ is relatively constant in depth for both episodes, in agreement with the LES results, the depth-averaged value (to $x_3/H = 0.75$, the scaled depth range common to both ensembles) is significantly positive, rather than zero, in both ensembles. This result led us to re-examine the assumption that the long axes of LSC are strictly parallel to the wind (granted, as argued previously, that the wind direction at the measurement site is known reasonably accurately, say to within 2°–3°, from the tower measurements). What angle between the wind direction and the long axis of LSC will reduce the observed positive values of $\langle -u_2' u_3' \rangle_{x_3 t}^{ne}$ to zero, and what are the effects of such a rotation on the other stress components? Figure 11 shows results of rotations of the ensemble mean fields for the two episodes shown in figure 10 by (*a*) 8° and (*b*) 18° to the right of the wind direction, rotations that reduce the depth-averaged values of $\langle -u_2' u_3' \rangle_{x_3 t}^{ne}$ to zero in each case. (Similar values determined for individual records are quite variable within the two episodes considered here, as might be expected for different realizations of a complex turbulent flow. However, without exception, all of the records require rotations that are either zero or to the right-hand side of the wind in order to reduce $\langle -u_2' u_3' \rangle_{x_3 t}^{n}$ to zero.) While we cannot determine conclusively that the rotation required to reduce $\langle -u_2' u_3' \rangle_{x_3 t}^{ne}$ to zero implies LSC structures aligned to the right-hand side of an accurately known wind, rather than systematic bias of the wind at the observation site to the left of the wind at the shore tower, we

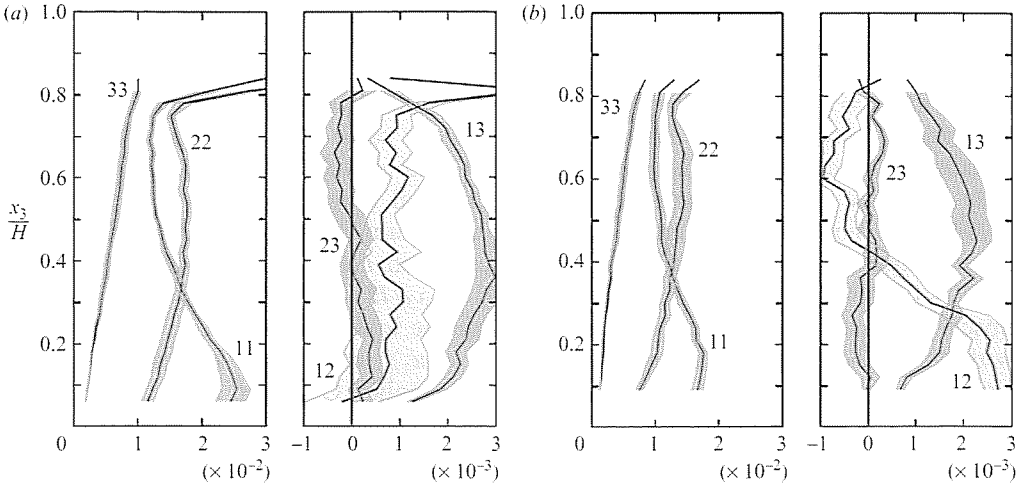

FIGURE 11. Profiles of ensemble-averaged normal (right-hand sides) and shear (left-hand sides) stress components and one standard deviation error bars for ensembles consisting of (*a*) eight records (023–030) from Session 43 and (*b*) five records (011–015) from Session 154. Velocity fields in the records making up each ensemble have been rotated (*a*) 8° and (*b*) 18° to the right of the record mean wind direction, rotations that result in zero depth-averaged $\langle -u_2'u_3' \rangle_{x_3t}^{ne}$. Labels as in figure 10.

tentatively accept the former interpretation as consistent with what is known of the representativeness of the tower winds, as well as with previous observations (Faller 1964, Smith *et al.* 1987; Weller & Price 1988) which report alignment of deep water Langmuir circulations either along or somewhat to the right of the wind.

The rotation required to reduce $\langle -u_2'u_3' \rangle_{x_3t}^{ne}$ to zero has rather little influence on the profiles of the normal stresses or of the $\langle -u_1'u_3' \rangle_{x_3t}^{ne}$ shear stress component, which can thus be considered as reliably determined independent of an unknown but small offset between wind and cells. It is then of interest to compare $\langle -u_1'u_3' \rangle_{x_3t}^{e}$, the (dimensional) downwind stress measured within the water column, with that applied by the wind at the sea surface. For the comparison we use Session 154, which we have argued provides the most reliable quantitative values, and restrict averaging to records 011 through 013, a period of very constant wind stress, $\tau_s = 0.19 \pm 0.01\ \mathrm{N\,m^{-2}}$. For this smaller ensemble, $\langle -u_1'u_3' \rangle_{x_3t}^{e} = 2.0 \times 10^{-4}\ \mathrm{m^2\,s^2}$ and the resulting in-water value of $\tau_0 = \rho_0 \langle -u_1'u_3' \rangle_{x_3t}^{e} \sim 0.20\ \mathrm{N\,m^{-2}}$ is nearly identical to the estimated surface stress. This degree of agreement is doubtless fortuitous, given that the in-water observations do not include the upper $\sim 20\,\%$ of the water column, nor the very near-bottom region. However noting that the profiles of figure 10 do show $\langle -u_1'u_3' \rangle_t^{e}$ tending towards zero at the top and bottom of the measured part of the water column, and given the constancy of values of measured stress and U_1^c over the three records, it appears that the agreement between τ_s and τ_0 is probably close. Similar calculations for the other records in the two sessions shown in figures 10 and 11 confirm agreement within a factor of 2 between the two stresses.

A second difference from the LES results is that $\langle -u_1'u_2' \rangle_t^{ne}$ is significantly non-zero over most of the water column in both episodes, while this stress component is zero in the 'pure' LC represented by the LES. Observed non-zero values of $\langle -u_1'u_2' \rangle_t^{ne}$, variability of $\langle -u_1'u_2' \rangle_t^{ne}$ between individual records (not shown) and sensitivity of $\langle -u_1'u_2' \rangle_t^{ne}$ to small horizontal rotation of axes (figures 10 and 11) may arise from

the presence in the observations of non-zero crosswind mean flow that is absent in the simulations. As discussed previously, this crosswind flow has a tidal component, but probably also contains a significant contribution from pressure gradients arising from rotational effects in the presence of a lateral boundary. This situation of mean flow driven simultaneously by surface stress and pressure gradient would benefit from theoretical and/or numerical study.

Together, the observational features described in § 5.1 and the comparisons with Langmuir-forced LES lead us to conclude that the observations are well (and most simply) described as due to full-depth LC, lined up approximately downwind. In this case, horizontal cell spacing (defined as the distance between successive downwelling regions) may be estimated as $L_h = U_2 T_a$, where T_a is the time it takes a cell to advect past the instrument at crosswind speed U_2. For the quite regular cells of record 43.025, average $T_a = 8$ min; hence using the mid-channel value $U_2^c = 0.19\,\mathrm{m\,s^{-1}}$, horizontal cell sizes are $L_h \cong 90$ m, roughly equal to the dominant surface wavelength and approximately six times the vertical scale L_v, taken as record mean water column depth (15.6 m). This value of the transverse-vertical cell aspect ratio L_h/L_v lies midway between values of ~3 previously found in deep-water (Smith *et al.* 1987; Weller & Price 1988) and higher values reported for shallower waters: Hunter & Hill (1980) report values of 6–25 for ~10 m water depth, while Marmorino *et al.* (2004) calculate a ratio of 10 in water of depth ~2 m. Other LSC records produce ratios within a range of 3–6, i.e. observed average ratio values are sometimes lower, but generally not higher, than 6, while the accompanying LES yield values ~4. It should be remarked that in general, as would be expected of turbulent flows, cell velocity structure is not highly regular and thus the scale ratio of individual cells can vary widely.

5.3. *Lumley invariant maps*

With measurements of the full three-dimensional velocity field, we are able to calculate a diagnostic thus far unique to observational studies of ocean turbulence, the depth trajectory, or map, of Lumley invariants (Lumley 1978). Invariants are calculated over the part of the water column accessible to our observations, and plotted in a 'triangle' within which realizable turbulent flows must lie: the form shown in figure 12 is that defined by Pope (2000). The Lumley invariant map is the trajectory of appropriate powers of $\mathrm{II} = b_{ij}b_{ji}$ and $\mathrm{III} = b_{ij}b_{jk}b_{ki}$, the second and third invariants of the turbulence anisotropy tensor $b_{ij} = \langle u_i' u_j' \rangle / 2\bar{q} - \delta_{ij}/3$ where $\bar{q} = \langle u_i' u_i' \rangle / 2$ is the turbulent kinetic energy (the first invariant $\mathrm{I} = \mathrm{trace}(b_{ij}) = 0$). The quantity $\mathrm{II}^{1/2}$ is a measure of the magnitude of the anisotropy, while the position of the coordinate $(\mathrm{II}^{1/2}, \mathrm{III}^{1/3})$ is a measure of the shape of the anisotropy, so the Lumley invariant map is extremely sensitive to the underlying flow structures. The linear sides of the triangle represent axisymmetric turbulence, which is pancake-shaped (oblate spheroid) if $\mathrm{III} < 0$ and cigar-shaped (prolate spheroid) if $\mathrm{III} > 0$. Asymmetry disappears in the isotropic limit $\mathrm{II} \to 0$, $\mathrm{III} \to 0$ at the bottom vertex of the triangle. The upper curved boundary of the triangle represents two-component turbulence, ranging from isotropic two-component turbulence at the $\mathrm{III} < 0$ vertex to one-component turbulence at the $\mathrm{III} > 0$ vertex. Turbulent boundary layers driven purely by surface stress have a depth trajectory that begins (at the wall) along the upper curved boundary, moves first towards the upper right-hand corner, then down along the right-hand boundary of the triangle towards the bottom 'isotropic' vertex as distance from the wall increases, returning towards the upper right-hand vertex as the surface is approached. Surface-stress-forced LES reproduces this behaviour (see Part 2), as do results from DNS of channel flow (Kim, Moin & Moser 1987, as shown in Pope 2000, figure 11.1).

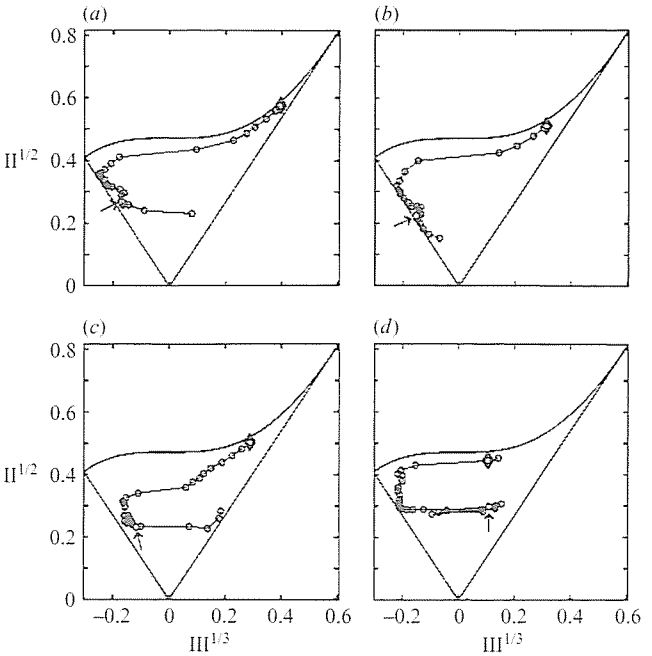

FIGURE 12. Depth trajectories built from the Lumley invariants $\mathrm{II} = b_{ij}b_{ji}$ and $\mathrm{III} = b_{ij}b_{jk}b_{ki}$, for records containing LSC: a diamond marks the measurement level closest to the ocean bottom, a small arrow indicates the level above which acoustic sidelobe effects are possible (although not obviously present) in slant beam data used to calculate horizontal velocity components. The Lumley 'triangle' shown is the form given by Pope (2000) and contains all realizable turbulent flows. LES simulations show that the 'C-shaped' trajectory is characteristic of surface stress-driven flow only when Langmuir forcing is included. As expected from associated values of La_b (§ 5), the shape of the observed trajectories is independent of the sign of surface buoyancy flux B_0. (*a*) 154.014, $La_t = 0.72$, $La_b = 0.0061$ ($B_0 > 0$), (*b*) 043.023, $La_t = 0.47$, $La_b = -0.0055$, $B_0 < 0$, (*c*) 043.025, $La_t = 0.48$,$La_b = 0.0043$ ($B_0 > 0$), (*d*) 043.026, $La_t = 0.52$, $La_b = 0.0057$ ($B_0 > 0$).

The traces of the LSC observations shown in figure 12 are a startling contrast, beginning near the upper boundary, but curving outwards towards the left-hand triangle boundary before turning back (usually) towards the right-hand boundary. While individual realizations of LSC flows differ in details (as seen in figure 12), most display this characteristic 'C' shape in the bottom third of the water column, behaviour only observed in the accompanying LES of Part 2 when C-L vortex forcing is present.

The observations differ somewhat from the LES results, particularly above mid-depth in the water column. Mid-channel values approach, but are not usually found right at the right-hand boundary as in the LES, and the observational trajectory only rarely doubles back towards the left-hand boundary in the upper half of the water column (at least the part of it accessible to the observations), as is observed in the Langmuir-forced LES. In cases where this latter behaviour is observed (e.g. figure 11*d*), it appears only if we include data from the upper 15 % of the (minimum) water column depth, some of which may possibly be contaminated by sidelobe reflections. Differences between observations and LES in the upper part of the water column may arise from the tidally variable surface height of the observational water column and/or the presence of surface-wave-generated turbulence, both effects absent in the

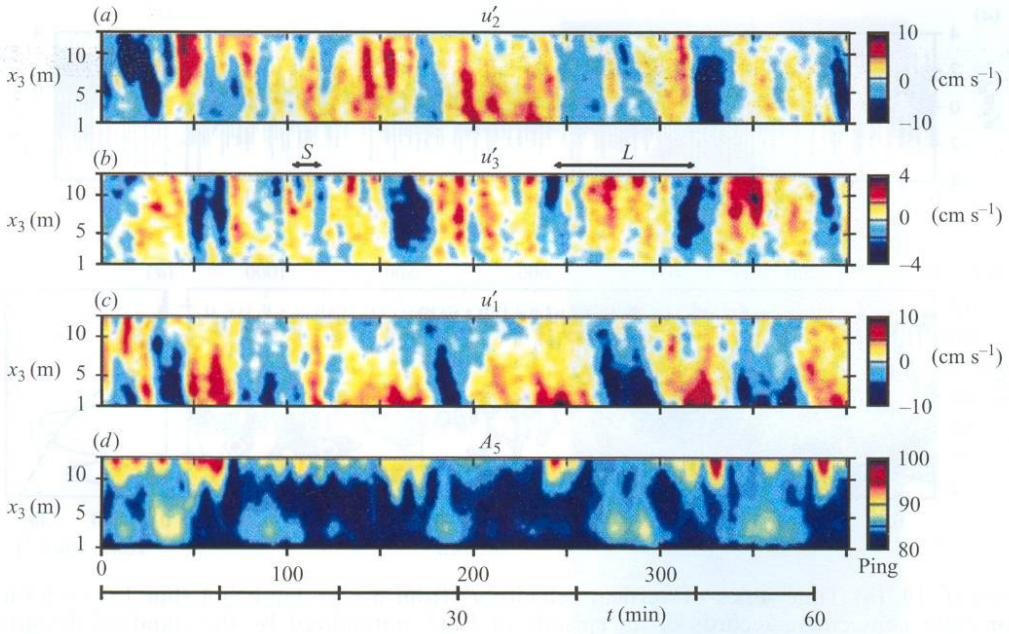

FIGURE 13. An enlarged portion of record 43.024 illustrates the existence of two distinctly different space/time scales of variability, clearly visible in both velocity and backscatter fields, during periods of LSC. The longer period (~8–17 min) features (L), identified here as LSC, are modulated by shorter period (~1–1.5 min) variability (S).

LES. Despite these caveats, the agreement of the distinctive depth trajectories of Lumley invariants between the observed LSC flows and LES with Langmuir forcing appears robust in the lower half of the mean water column.

6. Multiple scales in shallow-water Langmuir turbulence

Finally, we document a feature of the LSC observations that is absent from the associated LES, namely the existence of two distinct and significant scales in the velocity and backscatter fields. These are clearly visible in the colour presentation of figure 13, a section of record 43.024: any other LSC record could also be used to illustrate these two distinct scales. Features in both velocity and backscatter fields extending over ~50–100 pings (~8–17 min, marked 'L' in figure 13) are those associated with the large-scale structures that have been shown to exhibit many characteristics of LC. However, these features are clearly modulated by a much shorter scale of variability, of period typically ~6–10 pings (~1–1.5 min, marked 'S' in figure 13).

The distinctive periods involved are quantified by wavelet analysis of the time series seen in figure 14(*a*), that of u_3' from a mid-depth bin over the extent of approximately constant wind/wave forcing during the late spring episode of LSC (Session 43, records 23–30). To reduce the amount of detail in the figure, the wavelet power spectrum† Φ in figure 14(*c*) is presented with coarse grey scale: grey codes areas with $2 < \Phi < 16$

† The wavelet power spectrum was calculated using a Morlet basis function in wavelet software provided by C. Torrence and G. Compo at http://atoc.colorado.edu/research/wavelets.

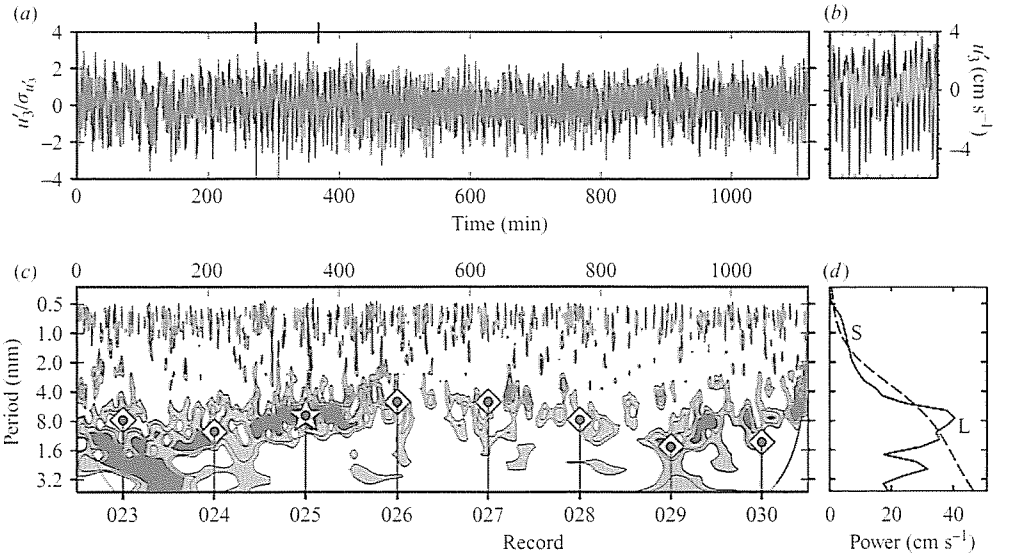

FIGURE 14. (*a*) Time series of vertical velocity u_3' from a mid-depth bin (bin 15, $z = 6.8$ m), for eight consecutive records of an episode of LSC, normalized by the standard deviation $\sigma_{u_3'} = 2.24\,\mathrm{cm\,s^{-1}}$ of the time series. (*b*) Expanded (unscaled) section of data corresponding to the time range marked on the upper boundary of (*a*)). (*c*) Wavelet power spectrum Φ, a function of period and time and (*d*) global wavelet spectrum Φ_g, with 95 % significance level (dashed line). The mid-points of records 43.023–43.030 are marked along the bottom axis of (*c*): vertical lines lead to symbols marking values of LSC 'period' predicted from measured record-mean crosswind velocities at mid-channel, assuming constant spatial scale equal to that of record 43.025, marked by a star.

$(\mathrm{cm\,s^{-1}})^2$ and black codes areas with $\Phi > 16$ $(\mathrm{cm\,s^{-1}})^2$. The global spectrum Φ_g in figure 14(*d*) is the average of the wavelet spectrum in figure 14(*c*) over the time extent of the record. A 95 % significance level calculated for the global spectrum indicates the existence of two significant temporal scales in u_3'. The shorter scale (S in figure 14*d*) corresponds to periods of ~(0.5–1.5) min, roughly that of the short-scale variability seen in figure 13. The S-scale appears to be period-invariant with time, at least in contrast with the longer time scale (L in figure 14*d*) which varies significantly in period over the extent of the records shown. Observed variations in this longer period can be roughly predicted by assuming that quasi-linear structures of fixed crosswind spatial scale, lined up approximately downwind, are being advected past the instrument by a mean crosswind flow that varies with the tides. Superimposed diamonds in figure 14(*c*) mark such periods, predicted for each record as $T = (T_0 U_0^c)/U_2^c$, where U_2^c is record mean crosswind velocity at mid-channel, and $T_0 \sim 7$ min, $U_0^c = 0.19\,\mathrm{m\,s^{-1}}$ are values for record 43.025 (star). This ability to predict the apparent period is strong additional support for the underlying assumption of structures that have fixed crosswind scale and are elongated in the downwind relative to the crosswind direction, i.e. structures consistent with Langmuir circulations. More complicated morphologies consistent with the observed periods are of course possible, but we think unlikely, given the consistency of the observational evidence described in this and previous sections.

7. Discussion and conclusions

This paper investigates three-dimensional flow structures associated with distinctive episodes of high-water column backscatter that occur during prolonged strong wind and wave forcing at a shallow continental shelf location. We have identified these structures as Langmuir circulations extending over the full depth of the water column, based first on several internally consistent qualitative characteristics of the measured flows, as follows.

Under approximately constant wind/wave forcing but variable tidal advection, the apparent periods observed at a fixed instrument are predicted most simply if the flow structures have a fixed crosswind scale and a larger downwind scale (§ 6). Although not detailed here, downwind elongation of sediment-bearing structures is also required to produce the consistent covariances observed among backscatter signals from the five VADCP beams when these are considered as an array. Thus structures exist with the morphology expected of the largest cells in Langmuir turbulence.

Accepting this basic structure and rotating the measured three-dimensional velocity field into wind coordinates, LSC exhibit many qualitative features that previous studies have identified as characteristic of LC:

(i) downwind jets situated under downwelling regions;

(ii) downwelling regions narrower than upwelling regions;

(iii) vertical asymmetry (surface intensification) of crosswind flows;

(iv) correct phasing of crosswind relative to vertical velocities, given the direction of crosswind advection past the fixed instrument;

(v) maximum vertical velocity in the upper half of the water column;

as described in § 5.1 and summarized in figure 7. The major qualitative difference from previous results is the strong near-bottom intensification of the downwind jets under downwelling regions, an effect absent in studies of deep-water LC and undoubtedly associated here with the presence of a (relatively) solid boundary.

Quantitatively, the formula of Li & Garrett (1997) provides an order of magnitude prediction of the maximum downwards vertical velocities observed as a function of wind speed measured at 10 m height, additional evidence for the identification as LC. However, maximum predicted vertical velocity does not correspond to maximum wind speed, suggesting a secondary sensitivity to details of the wind and/or surface wave fields.

In addition, we have compared the present observational results to companion results from LES (Part 2) carried out using stress and surface wave parameters derived from the observational conditions. This comparison is affected by various observational constraints (besides instrumental and sampling limitations) that do not enter the computations. The real-world observations took place in a complex environment that includes tidal flows (and may include rotational effects for some of the longer LSC events) in addition to the uni-directional (wind) stress-driven mean flow of the simulations. Also because of the tides, neither fluid depth nor 'mean' flow is constant in time. Surface gravity waves produce high-frequency variability that must be filtered out of the observed fluid velocities, a procedure that can only be carried out for a height above bottom that decreases as the mean surface falls with the tides. Increase in surface wave heights during the high winds/seas that accompany LSC further restricts the near-surface region accessible to the observations during these events, while wave breaking events may introduce additional turbulence, not modelled in the LES, to the accessible near-surface region. Flow very near the solid bottom boundary (which itself is neither exactly solid nor constant with time) cannot be measured because of the finite size of the VADCP. Finally, the observed fields

can be averaged only in time, not in time and horizontal flow dimensions as can be done for the LES results. Given all these constraints and differences, many of the characteristic features of LSC observations agree remarkably well, both qualitatively and often quantitatively, with results from Langmuir-forced LES:

(i) The observed three-dimensional flow structure is similar to that produced by LES runs with C-L vortex forcing added to surface stress forcing that, alone, produces basic Couette flow with very different morphology of turbulent structures.

(ii) Scaled vertical velocity variance has a maximum in the upper half of the water column, while downwind variance has a near-bottom maximum. Crosswind variance is less than downwind variance near the bottom boundary, but increases to exceed it in the upper water column.

(iii) Profiles of $\langle -u_1' u_3' \rangle_t^n$ are significantly different from zero.

(iv) Profiles of $\langle -u_2' u_3' \rangle_t^n \sim 0$ if the observational flow field is rotated by a small angle to the right of the wind.

(v) The character of Lumley invariant maps for observations and LES agree in the lower half of the water column, where they differ dramatically from the map of Couette flow, illustrating that the anisotropy of the energy-containing eddies is very different in these two cases.

The combined observational/LES study of Langmuir circulations forced by intermediate rather than deep-water waves has led to the realization that the effective magnitude of Langmuir forcing is not determined solely by the surface Stokes drift velocity, as expressed by the turbulent Langmuir number La_t, but is also a strong function of the depth structure of wave velocities, hence of the type of surface wave. Quantitative comparisons of observations with LES runs with different La_t also suggest the need for an improved estimate based on more extensive knowledge of the surface wave spectrum, possibly including its directional properties.

An important question is when Langmuir turbulence can be expected to dominate 'ordinary' turbulence generated in the bottom boundary layer of a tidal flow, as it does in the observations described here. As a rough metric, we ask how large the free-stream tidal velocity U_∞ must be in order to generate mid-depth r.m.s. turbulent velocity equal to that typical of the LSC observations. The r.m.s. tidal turbulent velocity is estimated using the relationship $\langle w'^2 \rangle = 1.61 u_*^2 \exp(-2x_3/H)$ with $u_*^2 = C_d U_\infty^2$ and $C_d = 2.5 \times 10^{-3}$ (Nezu & Nakagawa 1993) for open-channel flow. Setting this expression, evaluated at $x_3 = H/2$, equal to $4.5\,\mathrm{cm^2\,s^{-2}} = \langle u_3' u_3' \rangle$ for record 43.025 yields $U_\infty = 55\,\mathrm{cm\,s^{-1}}$. This value is consistent with the observed domination by Langmuir turbulence at LEO-15, where estimated maximum tidal flow is $\sim$20–25 $\mathrm{cm\,s^{-1}}$, but suggests that where tides are significantly stronger than $\sim$50–60 $\mathrm{cm\,s^{-1}}$, Langmuir turbulence will be increasingly disrupted by bottom boundary-layer turbulence.

The observations of LSC reported here suggest questions to be addressed by future observational and/or computational studies. For example, the question of what (if anything) sets the ratio of horizontal to vertical scales of the largest features remains an open one. In the present observations, typical ratios of $L_h/L_v \sim 5$–6 lie mid-way between values of $\sim$3–4 found for cells in deep-water (and in Van Straaten's (1950) very shallow-water regime) and values of $\sim$10 estimated in two cases of remote sensing observations of quasi-linear features in shallow ($H < 10\,\mathrm{m}$) water. Does this ratio have a limit under constant wind/wave forcing, or does the largest horizontal scale continue to increase as long as forcing is maintained, so that the dominant scale observed at any particular time is a function of integrated wind/wave history?

Another unknown is the process associated with the short time-scale fluctuations that are evident in visualizations of the observations and significant in the global

wavelet spectra of vertical velocity. (Additional evidence for multiple scales in Langmuir turbulence can be found in the deep-ocean dye and drifter observations of Assaf, Gerard & Gordon (1971) which revealed three distinct scales of convergence zones, and in the time-range patterns revealed by scattering from sub-surface bubble clouds (Thorpe 1992) which show large- and small-scale bands. Indeed, most observational studies of LC point to the existence of more than one scale of motion; however, the origin of the smaller scales remains unknown.) We think it most unlikely that the S-fluctuations in our measurements are associated with Couette cells typical of surface-stress-driven flows in the absence of C-L vortex forcing. First, the LES of Part 2 show that Couette cells disappear after Langmuir forcing is turned on, i.e. they do not coexist with the larger Langmuir cells that replace them. Secondly, if this fluctuation period were associated with turbulent structures advected by the mean crosswind flow, it too would exhibit the strong period variability shown in the wavelet analysis by the L-period features. Instead, the S-period is not noticeably affected by tidal variation in crosswind advection. Thus if the S-period is associated with a flow structure advecting past the VADCP (we consider the alternative hypothesis of non-propagation below), the process involved must have a characteristic horizontal crosswind speed much greater than those typically observed. A similar conclusion is that the S-period does not result from a downwind turbulent flow structure advected by the downwind mean flow since, owing to the presence of tides, the downwind mean flow is not routinely very much larger than the crosswind mean flow (and downwind scales are longer than crosswind scales). The apparent periods of 0.5–1.5 min are near those observed (in the unfiltered velocities) to be associated with 'groupiness' in the surface wave field. The group velocity of the surface waves at LEO-15, roughly half the phase speed, is still considerably larger than mean crosswind advection speeds, as required for invariance of apparent period. Thus, one possibility is that the S-period fluctuations are due to turbulent structures forced by variation in near-surface turbulence levels associated with group-induced surface-wave breaking, moving past the VADCP at the surface wave group velocity. An alternative possibility is that the S-period may not result from a propagating feature, but instead from events happening about once per minute at the measurement site. In this context, we note that Thorpe's (1992) measurements of the number of breaking waves as a function of 10 m wind speed predicts approximately one breaking wave per minute for the value of $U_{10} \sim 10\,\mathrm{m\,s^{-1}}$ typical of our measurements.

The discovery of frequent occurrences of LSC episodes during the unstratified part of the year on the shallow shelf at LEO-15 has profound implications for studies of the transport of sediment and bio-active material in similar shallow-sea environments. When LSC fill the water column, bottom material that has been resuspended in the high-shear, high-stress, but very thin, surface wave bottom boundary layer is efficiently moved out of low-speed near-bottom flow and introduced into the full downwind flow. In the cases presented here, even allowing for periodic reduction by adverse tidal flows, the net downwind flow is of the order of 0.3–$0.4\,\mathrm{m\,s^{-1}}$. Thus during a short one-day LSC event, material can be transported roughly 26–35 km, predominantly downwind. Moreover, since wind directions are relatively constant during LSC events, these downwind transports are highly directional, unlike those associated with oscillatory tidal flows. Because of the large distances involved, plus the highly directional nature of the transports associated with LSC episodes, a few major LSC events may accomplish most of the net transport of bottom-derived materials in well-mixed shallow seas. Since the LEO-15 observations show relatively little bottom-derived material present in the water column during the stratified (summer) portion

of the year, LSC events probably dominate the net annual transport of such materials at this location. LSC also carry bioactive material that may be of considerable importance to ecosystem function and biogeochemical cycling on shallow shelves. The strong bottom-to-surface vertical circulations of LSC provide a mechanism for episodic resupply of the surface layer with resting spores, bottom-incorporated but still viable phytoplankton, regenerated nutrients, etc., all introduced into the water column along with resuspended sediments. Strong and strongly directional horizontal transport associated with LSC events driven by the annual cycle of wind forcing may also provide a previously unsuspected vector for cross-shelf larval transports at crucial life stages (e.g. Checkley *et al.* 1988).

In conclusion, we believe that the observations reported here not only provide the most complete description yet published of the three-dimensional velocity structure associated with Langmuir circulations, but also reveal an important and previously unknown mechanism for transport of bottom-derived materials in shallow shelf seas.

We are grateful for research support from NSF (grant OCE-0136403) and NOAA (grant NA06RU0139), and the generous assistance of S. Glenn, O. Schofield and E. Creed. The success of the LEO-15 deployment was due to the technical expertise of C. Powell, and the support of R. Petrecca and the staff of the Rutgers Marine Field Station. S. Huang provided essential tools for data archiving and analysis. Detailed comments from two reviewers were very helpful.

REFERENCES

Assaf, G., Gerard, R. & Gordon, A. L. 1971 Some mechanisms of oceanic mixing revealed in aerial photographs. *J. Geophys. Res.* **76**, 6550–6572.

Checkley, D. M., Raman, S., Maillet, G. L. & Mason, K. M. 1988 Winter storm effects on the spawning and larval drift of a pelagic fish. *Nature* **335**, 346–348.

Craik, A. D. D. & Leibovich, S. 1976 A rational model for Langmuir circulations. *J. Fluid. Mech.* **73**, 401–426.

D'Asaro, E. A. 2001. Turbulent vertical kinetic energy in the ocean mixed layer. *J. Phys. Oceanogr.* **31**, 3530–3537.

Faller, A. J. 1964 The angle of windrows in the ocean. *Tellus* **16**, 363–370.

Faller, A. J. & Caponi, E. A. 1978 Laboratory studies of wind-driven Langmuir circulation. *J. Geophys. Res.* **83**, 3617–3633.

Gnanadesikan, A. 1996 Mixing driven by vertically variable forcing: an application to the case of Langmuir Circulation. *J. Fluid Mech.* **322**, 81–107.

Gargett, A., Wells, J. , Tejada-Martínez, A. E. & Grosch, C. E. 2004 Langmuir supercells: a mechanism for sediment resuspension and transport in shallow seas. *Science* **306**, 1925–1928.

Hunter, R. E. & Hill, G. W. 1980 Near-shore current pattern off south Texas: an interpretation from aerial photographs. *Remote Sensing Environ.* **10**, 115–134.

Kim, J., Moin, P. & Moser, R. 1987 Turbulence statistics in fully developed channel flow at low Reynolds number. *J. Fluid Mech.* **177**, 133–166.

Kohut, J. T., Glenn, S. M. & Chant, R. J. 2004 Seasonal current variability on the New Jersey inner shelf. *J. Geophys. Res.* **109**, C07S07. doi:10.1029/2003JC001963.

Langmuir, I. 1938 Surface motion of water induced by wind. *Science* **87**, 119–123.

Leibovich, S. 1983 The form and dynamics of Langmuir circulations. *Annu. Rev. Fluid Mech.* **15**, 391–427.

Lenschow, D. H., Mann, J. & Kristensen, L. 1994 How long is long enough when measuring fluxes and other turbulence statistics? *J. Atmos. Ocean. Technol.* **11**, 661–673.

Li, M. & Garrett, C. 1995 Is Langmuir circulation driven by surface waves or surface cooling? *J. Phys. Oceanogr.* **25**, 64–76.

Li, M. & Garrett, C. 1997 Mixed layer deepening due to Langmuir circulation. *J. Phys. Oceanogr.* **27**, 121–132.

LI, M., GARRETT, C. & SYKLLINGSTAD, E. 2005 A regime diagram for classifying turbulent eddies in the upper ocean. *Deep-Sea Res.* I **52**, 259–278. doi:10.1016/j.dsr.2004.09.004.

LOHRMANN, A., HACKETT, B. & ROED, L. P. 1990 High resolution measurements of turbulence, velocity, and stress using a pulse-to-pulse coherent sonar. *J. Atmos. Ocean. Tech.* **7**, 19–37.

LUMLEY, J. L. 1978 Computational modelling of turbulent flow. *J. Geophys. Res.* **88**, 123–176.

MCWILLIAMS, J. C., SULLIVAN, P. P. & MOENG, C.-H. 1997 Langmuir turbulence in the ocean. *J. Fluid Mech.* **334**, 1–30.

MARMORINO, G. O., SMITH, G. B. & LINDEMANN, G. J. 2004 Infrared imagery of large-aspect-ratio Langmuir circulation. *Contl. Shelf Res.* **25**, 1–6. doi:10.1016/j.csr.2004.08.002.

MÜNCHOW, A. & CHANT, R. J. 2000 Kinematics of inner shelf motions during the summer stratified season off New Jersey. *J. Phys. Oceanogr.* **30**, 247–268.

NEZU, I. & NAKAGAWA, H. 1993 *Turbulence in Open Channel Flows.* International Association for Hydraulic Research Monograph Series. A. A. Balkema, Rotterdam.

PLUEDDEMANN, A. J., SMITH, J. A., FARMER, D. M., WELLER, R. A., CRAWFORD, W. R., PINKEL, R., VAGLE, S. & GNANADESIKAN, A. 1996 Structure and variability of Langmuir circulation during the surface waves processes program. *J. Geophys. Res.* **101**, 3525–3543.

POLLARD, R. T. 1976 Observations and theories of Langmuir circulations and their role in ocean mixing. In A Voyage of Discovery, George Deacon 70th Anniversary Vol., *Deep-Sea Res (Suppl.)*, pp. 235–251.

POPE, S. B. 2000 *Turbulent Flows.* Cambridge University Press.

SKYLLINGSTAD, E. D. & DENBO, D. W. 1995 An ocean large-eddy simulation of Langmuir circulations and convection in the surface mixed layer. *J. Geophys. Res.* **100**, 8501–8522.

SMITH, J., PINKEL, R. & WELLER, R. A. 1987 Velocity structure in the mixed layer during MILDEX. *J. Phys. Oceanogr.* **17**, 425–439.

SMITH, J. A. 1992 Observed growth of Langmuir circulation. *J. Geophys. Res.* **97**, 5651–5664.

TEJADA-MARTÍNEZ, A. & GROSCH, C. E. 2007 Langmuir turbulence in shallow water. Part 2. Large-eddy simulations. *J Fluid Mech.* **576**, 63–108.

TENNEKES, H. & LUMLEY, J. L. 1972 *A First Course in Turbulence.* The MIT Press, Cambridge MA.

THORPE, S. A. 1992 Bubble clouds and the dynamics of the upper ocean. *Q. J. R. Met. Soc.* **118**, 1–22.

THORPE, S. A. 2004 Langmuir circulation. *Annu. Rev. Fluid Mech.* **36**, 55–79.

THORPE, S. A. & HALL, A. J. 1983 The characteristics of breaking waves, bubble clouds, and near-surface currents observed using side-scan sonar. *Continent. Shelf Res.* **1**, 353–384.

TROWBRIDGE, J. H. & AGRAWAL, Y. C. 1995 Glimpses of a wave boundary layer. *J. Geophys. Res.* **100**, 20 729–20 743.

VAN STRAATEN, L. M. J. U. 1950 Periodic patterns of rippled and smooth areas on water surfaces, induced by wind action. *Koninklijke Ned. Akad. van Wetenschappen Proc.* **53**, 1217–1227.

WELLER, R. A. & PRICE, J. F. 1988 Langmuir circulation within the oceanic mixed layer. *Deep-Sea Res.* **35**, 711–747.

ZEDEL, L. & FARMER, D. M. 1991 Organized structures in subsurface bubble clouds: Langmuir circulation in the open ocean. *J. Geophys. Res.* **96**, 8889–8900.